TAMPERE UNIVERSITY OF TECHNOLOGY

JUSSI SIHVO

INTERNAL IMPEDANCE MEASUREMENT TECHNIQUES AND CHARGER DYNAMICS FOR LITHIUM-ION BATTERIES

Master's Thesis

Examiners:
Assistant Prof. Tuomas Messo
Examiners and topic approved by the
Faculty Council of the Faculty of
Computing and Electrical-Engineering
on the 20th of November 2017

ABSTRACT

JUSSI SIHVO: Internal impedance measurement techniques and charger dynamics for lithium-ion batteries
Tampere University of Technology
Master's Thesis, 76 pages
November 2017
Master's Degree Programme in Computing and Electrical Engineering
Major: Power Electronics
Examiners: Assistant Prof. Tuomas Messo
Keywords: BESS, battery internal impedance, SOC, SOH, PRBS, CC-CV, bi-directional DC-DC converter, load-effect, source-effect

The increasing popularity of renewable energy is already given rise to a concept of energy storage system (ESS) which to be installed in pursuance of renewable energy power plant. This is done to provide compensation to RES energy production which fluctuates due to the constantly changing wheather conditions. Battery energy storage systems (BESS) with Lithium-ion technology is attracting alternative for ESS since batteries have relatively high energy density.

Batteries are monitored in terms of state of charge (SOC) and state of health (SOH). The exact estimation of these quantities is quite problematic due to the unpredictability of chemical reactions taking place inside the battery. One characteristic providing information about them both is the battery internal impedance which respond varies at different frequencies as a function of SOC and SOH. Battery internal impedance measurements are therefore of great importance and electrochemical impedance spectroscopy (EIS) is mostly used in this purpose in laboratory environment. Attractive alternative for excitation signal is pseudo random binary sequence (PRBS) which has potential of be used online monitoring of internal impedance.

Battery internal impedance can also be considered as source- and load effect to the battery charger which is a bi-directional DC-DC converter. It is not widely investigated how internal impedance affects to the converter control loop at different control modes.

This thesis presents battery impedance measurements with PRBS excitation signal which results are compared to results obtained by original EIS-related sine sweep excitation signal. The measured internal impedance is further used to simulate the source- and load effect and it's impact on the bi-directional DC-DC converter operation at different control modes.

TIIVISTELMÄ

JUSSI SIHVO: Sisäisen impedanssin mittaustavat ja laturin dynamiikka litiumioni akuissa
Tampereen Teknillinen Yliopisto
Diplomityö, 76 sivua
Marraskuu 2017
Sähkötekniikan diplomi-insinöörin tutkinto-ohjelma
Pääaine: Tehoelektroniikka
Examiners: Assistant Prof. Tuomas Messo
Avainsanat: Akun sisäinen impedanssi, akun varaustila, akun terveys, PRBS

Energiavarastot ovat tulevaisuudessa suosittuja uusiutuviin energianmuotoihin pohjautuvien sähkövoimaloiden yhteydessä. Energia varastoilla voidaan tasoittaa uusiutuvilla energianlähteillä tapahtuvaa tuotetun tehon vaihtelua, sillä sähköverkkoon halutaan aina mahdollisimman tasaista tehoa. Erityisesti akkuvarastot ovat tutkittuja energiavarastoteknologioita sillä niiden energia ja tehotiheys on suhteellisen suuri.

Akkujen ennustettavuus on kuitenkin hankalaa sillä kemialliset reaktiot akun sisällä tapahtuvat aina hieman eri tavalla riipuen monista tekijöistä. Akuista tarkkaillaan yleensä varaustilaa ja terveyttä, joiden estimointiin voidaan käyttää akun sisäistä impedanssia. Tämän vaste eri taajuuksilla muuttuu akun varaustilan ja terveyden funktiona. Elektrokemiallista impedanssi spektroskopiaa on laboratorio-olosuhteissa laajalti käytetty akun impedanssin mittaamiseen. Samaan tarkoitukseen käytetään tässä työssä binääristä PRBS herätesignaalia.

Mitattua akun sisäistä impedanssia käytetään lopuksi analysoimaan akun impedanssin parasiittisia vaikutuksia akun laturin kuormana ja lähteenä. Analysointi on toteutettu simulointeina oikeasta impedanssin mittausdatasta käyttäen eri ohjausmenetelmää akun tasavirtalaturille.

CONTENTS

1. Introduction 1

2. Energy storage systems and their different configurations 3

3. Battery storages 6

3.1 Battery SOC and SOH 7

3.2 Internal impedance of the battery 8

3.3 Lithium-ion Batteries 9

3.4 Battery modeling 11

3.4.1 Linear model 12

3.4.2 Randles' model 12

3.4.3 A controlled voltage source battery model 13

3.4.4 Discussion of the models 17

4. Battery internal impedance measurement techniques 18

4.1 System identification 18

4.2 Excitation signals 19

4.2.1 Sine sweep 20

4.2.2 Pseudo random binary sequence (PRBS) 21

4.3 Battery internal impedance measurements 23

4.3.1 Laboratory setup 23

4.3.2 Optimizing parameters for excitation signals 25

4.4 Measurement results 26

4.5 Analysing the Results 31

4.6 Estimation of linear transfer function from the measurement results . 31

5. DC-DC converter for BESS 34

5.1 Choosing the topology for the bi-directional DC-DC converter 34

5.2 Modeling of the bi-directional buck-boost DC-DC converter in CCM . 34

5.2.1 Modeling of the boost-mode 36

5.2.2 Modeling of buck-mode 41

5.3 Control scheme for the bi-directional DC-DC converter 47

5.3.1 Loop-shaping technique for control design 47

5.3.2 Current control for discharge of the battery (without source- and load effect) 50

5.3.3 CC-control for charge of the battery (without source- and load effect) 52

5.3.4 CV-control for charge of the battery (without source- and load effect) 54

5.4 Load and Source-Effect of Battery to DC-DC Converter 54

5.4.1 Source effect of the battery impedance in boost mode 55

5.4.2 Load effect of the battery impedance in buck-mode (CC) 57

5.4.3 Load effect of the battery impedance in buck-mode (CV) 59

6. Simulations 63

6.1 Converter simulations without load- and source effect 65

6.2 Converter simulations with load- and source effect included 67

7. Conclusions 70

SYMBOLS

Small-signal symbols

$\hat{i}_{bat}$	Battery current
$\hat{i}_c$	Capacitor current
$\hat{i}_{DC}$	DC-link current
$\hat{i}_L$	Inductor current
$\hat{v}_{bat}$	Battery voltage
$\hat{v}_{batL}$	Source affected battery voltage
$\hat{v}_{batS}$	Source affected battery voltage
$\hat{v}_C$	Capacitor voltage
$\hat{v}_{DC}$	DC-link voltage
$\hat{d}$	duty ratio

Other symbols

A	Battery voltage exponential zone amplitude
a	Amplitude
B	Battery exponential zone time constant inverse
$b(t)$	System excitation signal as a function of time
C	Capacitance
D	Duty ratio steady-state
D'	Duty ratio complement steady-state
d	Duty ratio
E	Source voltage
E_0	Battery constant voltage
E_{full}	Battery source voltage at fully charged point
E_{exp}	Battery source voltage at the end of exponential zone
E_{nom}	Battery source voltage at the end of nominal zone
f	frequency
f_{cross}	Cross-over frequency
f_{gen}	Generating frequency
f_{res}	Frequency resolution
f_s	Sampling frequency
f_{sw}	Switching frequency
$G_{batDC-o}$	Open-loop battery-to-DC-link transfer function

G_{CO}	Control-loop transfer function
$G_{cbat-load-o}$	Open-loop load-affected control-to-battery transfer function
G_{cbat-o}	Open-loop control-to-battery transfer function
G_{cc}	Controller transfer function
$G_{cDC-load-o}$	Open-loop load-affected control-to-DC-link transfer function
G_{cDC-o}	Open-loop control-to-DC-link transfer function
G_{ci-o}	Open-loop control-to-input transfer function
G_{co-o}	Open-loop control-to-output transfer function
$G_{DCbat-load-o}$	Open-loop load-affected DC-link-to-battery transfer function
$G_{DCbat-o}$	Open-loop DC-link-to-battery transfer function
G_{io-o}	Open-loop input-to-output transfer function
$G(j\omega)$	System transfer function frequency response
$g(t)$	System impulse response as a function of time
I_{bat}	Battery current steady-state
I_L	Inductor current steady-state
$I(j\omega$	Current frequency response
i_{bat}	Battery current
i_{DC}	DC-link current
i_{in}	Converter input current
i_{inS}	Converter source-affected input current
i_L	Inductor current
i_{meas}	Measured Battery current
i_{out}	Converter output current
i_{outL}	Converter load-affected output current
i_{ref}	Battery current reference
j	Imaginary unit
K	Battery polarization constant
K_{cc}	Controller gain
K_I	Integral gain
K_P	Proportional gain
L	Inductance
M	Averaging periods
N	Length of PRBS sequence in samples
n	Number of shift registers used for PRBS generation
P_{ref}	Power reference
Q	Charge extracted from battery
Q_0	Nominal capacity of battery
Q_{exp}	Consumed battery charge at the end of exponential zone
Q_{nom}	Consumed battery charge at the end of nominal zone

q	Sequence number
R_{eq}	Equivalent resistance term
R_{int}	Internal resistance
r_C	Capacitor parasitic resistance
r_D	Diode parasitic resistance
r_DS	Switch parasitic resistance
S	Switch
s	Laplace variable
SOC	State of charge
$T_{batDC-o}$	Open-loop battery-to-DC-link transmittance
$T_{DCbat-o}$	Open-loop DC-link-to-battery transmittance
$T_{batDC-load-o}$	Open-loop load-affected battery-to-DC-link transmittance
T_{meas}	Measurement time
T_{oi-o}	Open-loop output-to-input transmittance
t	time
$U(j\omega)$	Voltage frequency response
V_{bat}	Battery terminal voltage steady-state
$V_{bat-thresh-20\%}$	CV-control mode threshold for 20% SOC
$V_{bat-thresh-75\%}$	CV-control mode threshold for 75% SOC
V_C	Capacitor voltage steady-state
V_D	Diode forward voltage
V_{DC}	DC-link voltage steady-state
V_{eq}	Equivalent voltage term
V_{in}	Input voltage steady-state
V_{meas}	Measured battery terminal voltage
V_{OCV}	Battery open-circuit voltage
V_{out}	Output voltage steady-state
v_{bat}	Battery terminal voltage
v_C	Capacitor voltage
v_{DC}	DC-link voltage
v_{in}	Converter input voltage
v_{inS}	Converter source-affected input voltage
v_L	Inductor voltage
v_{out}	Converter output voltage
v_{outL}	Converter load-affected output voltage
v_{ref}	Voltage reference
$X(j\omega)$	System input signal frequency response
$x(t)$	System input signal as a function of time
Y_{bat-o}	Open-loop battery-side admittance

Y_{DC-o}	Open-loop DC-link admittance
$Y_{DC-load-o}$	Open-loop load-affected DC-link admittance
Y_{in-o}	Open-loop input admittance
$Y(j\omega)$	System output signal frequency response
Y_{o-o}	Open-loop output admittance
$y(t)$	System output signal as a function of time
Z_{bat}	Battery impedance
$Z_{bat-load-o}$	Open-loop load-affected battery-side impedance
Z_{bat-o}	Open-loop battery-side impedance
$Z_{j\omega}$	Impedance frequency response
Z_L	Battery load impedance
Z_S	Battery source impedance
$Z_{SOC-75\%}$	Battery impedance at 75% SOC
$Z_{SOC-20\%}$	Battery impedance at 20% SOC
z^{-1}	Unit delay
ϕ	Phase angle
ω	Angular frequency
ω_p	Pole angular frequency
ω_z	Zero angular frequency

ABBREVIATIONS

BESS	Battery energy storage system
BMS	Battery management system
CCM	Continuous conduction mode
CC-CV	Constant-current constant-voltage
CF	Current-fed
CO	Current-out
DC	Direct current
DCM	Discontinuous conduction mode
DFT	Discrete fourier-transform
DG	Distributed generation
DOD	Depth of discharge
EIS	Electrochemical impedance spectroscopy
ESS	Energy storage system
FFT	Fast fourier transform
GM	Gain margin
HESS	Hybrid energy storage system
KCL	Kirchhoff's current law
KVL	Kirchhoff's voltage law
LCO	Lithium cobolt oxide
LFP	Lithium iron phosphate
LHP	Left half plane
LMO	Lithium manganese oxide
LTI	Linear time-invariant
MLBS	Maximum length binary sequence
MPPT	Maximum powerpoint tracking
NMC	Lithium nickel manganese cobolt oxide
OCV	Open-circuit voltage
PI	Proportional-integral
PM	Phase margin
PRBS	Pseudo random binary sequence
PV	Photovoltaic
PWM	Pulse width modulation
RES	Renewable energy resource
RHP	Right half plane
SNR	Signal-to-noise ratio
SOC	State of charge

SOH	State of health
VF	Voltage-fed
VO	Voltage-out

1. INTRODUCTION

Renewable energy sources (RES) are nowadays already taken root in the energy production worldwide mostly due to global warming. Depletion of fossil fuels and growing awareness in the importance of making clean and renewable energy with low greenhouse gas emissions will make RES even more popular in the future. Possibility to produce electricity locally has given rise to a concept of distributed generation (DG). In DG, energy production is centralized in microgrids that can either act as a separate DG unit (island) or a part of the main power grid. This development will drastically change the power production and also the power infrastructure in the future while it is still today mostly based on non-renewable natural sources such as fossil fuels and nuclear energy.

Power production in RES is totally dependent on the dominant weather conditions which can vary a lot within a relatively short period of time. However, within these periods, power demand in the grid is often constant which means that there will be a power mismatch between generation and load. In order to satisfy the power demand in grid, an energy storage system (ESS) can be connected in parallel as a back-up power source. ESS can both produce power in underproduction situation and store power when RES produces more power than grid demands. Considering ESS applications with RES, secondary batteries and battery energy storage systems (BESS) are popular and widely investigated for this purpose in the literature [1–3]. This is due to their matured technology and high energy density which allows ESS to provide energy for the grid even in deep underproduction conditions.

Challenging aspect is, however, the exact estimation of battery state due to the chemical reactions taking place inside the battery. These reactions will change under varying ambient conditions and as a result of aging. Many concepts, i.e. state of charge (SOC) and state of health (SOH) has been introduced to realize the state of the battery. SOC indicates how much energy battery can provide until it needs to be recharged and SOH indicates the age of the battery and when it should be replaced. Both of these can be constantly monitored by battery management system (BMS) integrated into the battery. It has been shown that these quantities are related to internal impedance of the battery with the extent depending on the

battery chemistry. [4, 5]

To measure battery impedance, electrochemical impedance spectroscopy (EIS) is widely used and commercialized method. Other perturbation signals such as square pulse and pseudo random binary sequence (PRBS) are also introduced in literature for obtaining frequency response of battery internal impedance [6–8]. PRBS method's suitability for battery applications will be more investigated in this thesis.

In many publications, internal impedance of a battery is used to obtain parameters for battery models of various kinds. However, battery internal impedance effect on the dynamics and stability of the DC-DC converter and the whole DG unit has not been investigated widely in the literature. A concept of 'source- and load effect' is already been introduced for DC-DC converters with EMI filter as source and has been shown to affect on the stability of the converters. This concept is here used to observe the damping effect of internal impedance on the DC-DC converter. [9, 10]

This thesis is divided into seven sections. After introduction, second section concentrates on the principal structure of RES with ESS and also the structure of ESS used in this thesis is introduced. Battery chemistries and battery models are presented and selected for the thesis purposes in section three. In section four, methods for measuring battery impedance are introduced. Section five applies to modeling and control of the DC-DC converter in between the BESS and DC-link of RES with and without source-and load effect. Simulations are carried out in the section 6 and conclusions are at last made in section seven. The main contribution of this thesis is however the battery impedance measurement techniques and especially the PRBS method which is not widely investigated for battery applications in the literature.

2. ENERGY STORAGE SYSTEMS AND THEIR DIFFERENT CONFIGURATIONS

ESS should have high energy- and power density to be able to provide relatively high power for a long time. This holds also for charging which is desired to be fast enough when there is power available in RES. Promising ESS technologies to both produce and store power are i.e. secondary batteries, super-capacitors [11] and hydrogen technology [12].

However, high energy density often comes with the expense of low power density and vice versa. For instance, super-capacitors have high power density but relatively low capacity whereas secondary batteries have high capacity but cannot provide as high power without significant losses as same scale super-capacitors. Such dilemma can be overcome by linking different ESS technologies together. Such system is then called hybrid energy storage system (HESS) [11–13].

The insertion of ESS often requires a bi-directional converter that controls the direction of power flow and adjusts the voltage level appropriate for the output. Altogether, there are different converter topologies that can be used. When considering a photovoltaic (PV)-power plant, different connections of ESS are illustrated in figures 2.1 and 2.2 for single-stage and double-stage PV-power plant.

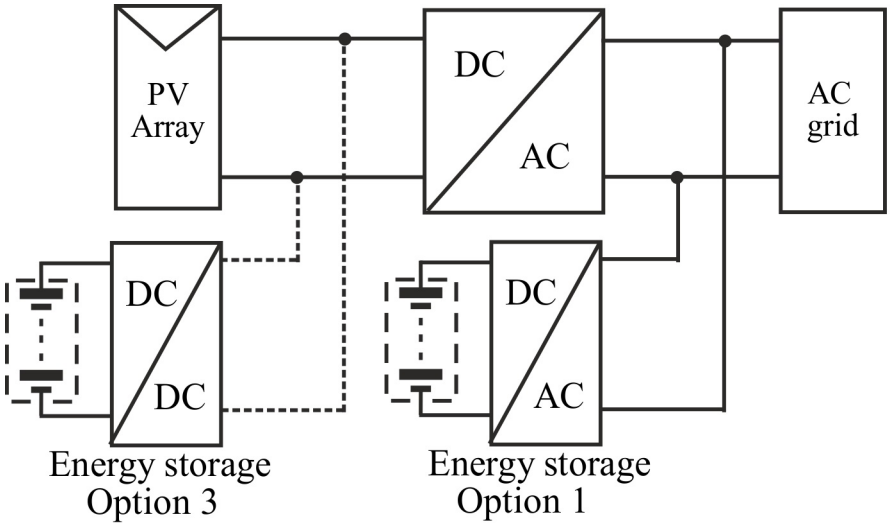

Figure 2.1 *Different ESS connections to single-stage PV-power plant*

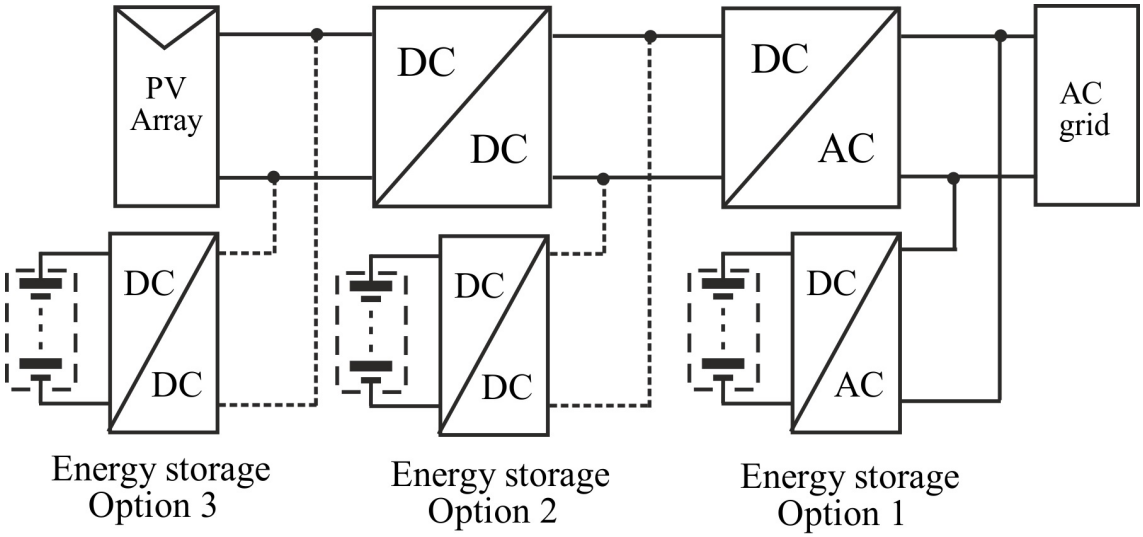

Figure 2.2 *Different ESS connections to double-stage PV-power plant*

For PV-power plants, single-stage connection is made with an inverter only. Double-stage connection requires an extra converter cascaded with the inverter. Double-stage connection is often required because of the need of maximum-power-point-tracking (MPPT) of PV-panels [14]. PV-panels' output current is a function of their output voltage which is controlled to the maximum-power-point (MPP) with a DC-DC converter between the PV-array and inverter.

In double-stage system (figure 2.2), energy storage option 1 is connected straight to the grid with inverter [3]. In option 2 [1, 2], ESS is connected to the inverter DC-link of the PV-generator. For option 3, ESS configuration is similar to that in

option 2 but connection is at the PV-generator's MPPT-converter input side. In the economic point of view, option 2 is the most optimal choice since both PV-array and ESS uses the same inverter and power never needs to flow towards the PV-array which yields that the DC-DC converter can be uni-directional. It is also regarded as more efficient topology in [15].

Due to the reasons listed above, double-stage PV-power plant with energy storage option 2 in figure 2.2 is further considered in this thesis. However, the modeling of PV-array, inverter and the DC-DC converter in between them are out of the context of this thesis. The part that is on the focus in this thesis is shown in figure 2.3.

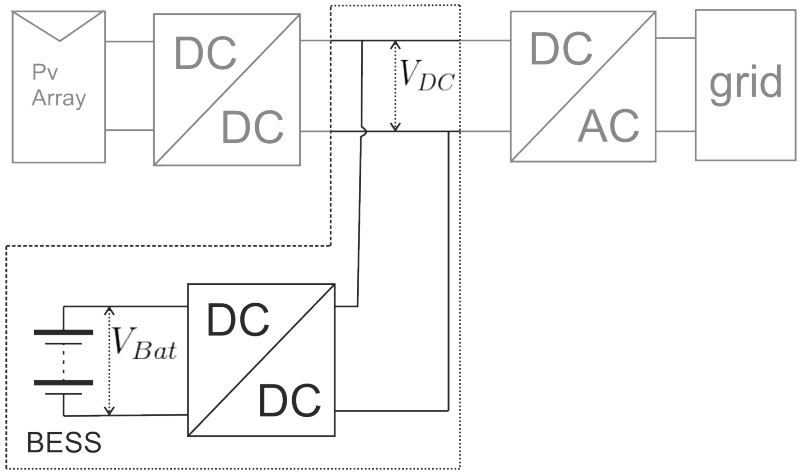

Figure 2.3 *Part of the double-stage RES with chosen ESS connection for the thesis*

The DC-link is modeled with stiff constant voltage which can be considered irrelevant approximation. However, since the focus is more on the battery impedance and it's effect on the bi-directional DC-DC converter, such simplification is considered to be appropriate.

3. BATTERY STORAGES

Battery is a device that stores electrical energy through chemical reactions. These reactions are taking place in the positive electrode and negative electrode of the battery cell resulting in a circulating current when both electrodes are connected with a conductor. Principal elements and reactions taking place inside battery cell are shown in figure 3.1.

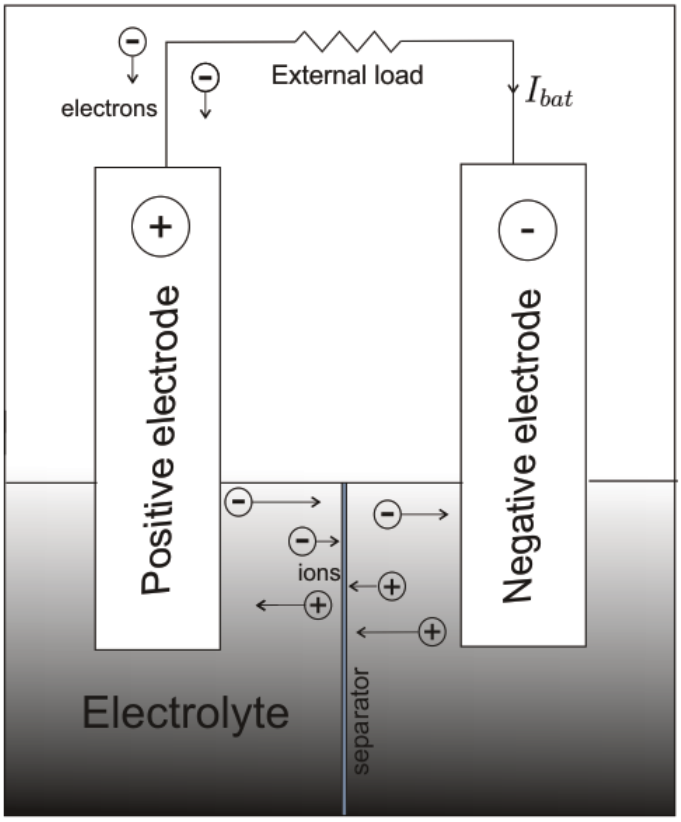

Figure 3.1 *Principal scheme of the battery cell reactions (galvanic cell)*

In figure 3.1 battery cell, positive- and negative electrodes are placed in electrolyte which can carry ions between the electrodes. Electrolyte is, however, not electrically conductive since this would result in short-circuit between the electrodes. Both electrodes undergoes a half-cell reaction that together results in a potential difference between the electrodes. When connecting electrodes with external conductor, cur-

rent starts to flow with electrons flowing in the opposite direction. This results also as ion exchange through electrolyte with positive ions (cations) carrying towards positive electrode and negative ions (anions) towards the negative electrode. [16]

In reality, batteries consists of multiple individual battery cells since terminal voltage and capacity of one cell is too low for many realistic application. Battery terminal voltage can be raised by connecting cells in series while capacity can be raised with parallel connection of the cells or strings. Such connections requires a balancing circuit driven by BMS to avoid significant losses and even hazardous operation of a battery when individual cells in strings gets defective. [17, 18]

Batteries can be coarsely divided into two categories, primary and secondary batteries. In primary batteries, chemical reactions are taking place uni-directionally which means that primary batteries can only be discharged (galvanic cell). Secondary batteries' chemistry works bi-directionally so that they can be charged (electrolytic cell) and discharged in cycles. In terms of ESS, secondary batteries are doubtlessly used due to their sustainability which is why they are also further discussed in this thesis. Reactions in both cell types with same chemistry are reversible and reactions can be represented as follows.

Negative electrode:

$$\mathrm{M} \underset{\text{charge}}{\overset{\text{discharge}}{\rightleftharpoons}} \mathrm{M}^{n+} + \mathrm{ne}^{-} \tag{3.1}$$

Positive electrode:

$$\mathrm{nX} + \mathrm{ne}^{-} \underset{\text{charge}}{\overset{\text{discharge}}{\rightleftharpoons}} \mathrm{nX}^{-} \tag{3.2}$$

During discharge, metal M in negative electrode (3.1) oxidizes as a result of half-cell reaction. As a result, positive electrode also undergoes a half-cell reaction and metal-oxide X in 3.2 reduces. Phenomenons in 3.1 and 3.2 combined is called redox. These reactions are always taking place together and simultaneously. During charge, current applied from external source makes the reactions in battery electrodes to be reversed.

3.1 Battery SOC and SOH

Batteries available energy is usually defined with SOC. SOC indicates the remaining capacity of the battery as percentage of the rated capacity. Sometimes SOC inverse, Depth Of Discharge (DOD), is used to indicate the same measure. Conventional methods for SOC estimation are i.e. *Coulomb counting* and *voltage reading*

interpretation from the voltage-SOC look-up tables provided by the battery manufacturer. In Coulomb Counting method, battery current is integrated over time and checked against the nominal capacity of the battery. In mathematical form, it can be represented as follows.

$$SOC = (1 - \frac{Q}{Q_0})100\% \tag{3.3}$$

In (3.3) Q_0 is the nominal capacity of the battery and Q is the actual charge already extracted from the battery. The problem in both foregoing SOC estimation methods is the fact that they rely on a reference (capacity in Coulomb Counting and voltage in voltage reading method) that is assumed to be valid all the time. This is why above mentioned SOC estimation methods are highly inaccurate in real application but are often used as one part of the algorithm in more sophisticated methods that take many other quantities into account. These are i.e. C-rate, temperature, internal impedance and memory effect for some battery chemistries and these often tends to have non-linear impact on the SOC along with terminal voltage. State-of-the-art SOC estimation methods uses i.e. Kalman filter and neural networks as estimation tool or classifier [4].

Even though an algorithm could sufficiently enough estimate SOC for a start, it may not do so as the battery cycle life increases. Electrodes and electrolyte tends to frail as the battery cycle life increases. Also the way battery is used affects to it's life making the SOC estimation even more difficult. This aging of the battery is often indicated with a figure of merit called SOH that indicates when the battery life is coming to an end and should be replaced. It's definition, however, depends on the application that battery is designed for. I.e. batteries, that are indicated useless for electric vehicles according to their SOH, can still be used in ESS [19]. Thus SOH is much more abstract concept than SOC. SOH and SOC are both the outputs of the BMS that monitors battery state which is extremely important and demanding for lithium-ion batteries. [17, 18]

3.2 Internal impedance of the battery

Reactions taking place in a cell always involves losses. These losses are due to the internal impedance of the battery resulting the completed-circuit voltage of the battery being always lower than the open-circuit voltage during discharge. During charge the complete-circuit voltage is greater than open-circuit voltage by contrast. Thus internal impedance of the battery is desired to be as small as possible. Thus electrodes are in reality placed physically as close to each other as possible to minimize

the distance that ions need to travel between the electrodes. However, electrodes placed too close to each other may lead to a short-circuit between them. This is prevented by inserting a thin separator between the electrodes (also in figure 3.1) to prevent them from touching each other while still allowing ions to go through it. Internal impedance can be supposed to consists of two below-mentioned concepts.

- *Polarization losses*
- *Ohmic losses*

Polarization losses are perceived as the losses due to non-ideal reactions at the electrodes and electrolyte. These are i.e. kinetic limitations of the charge transferring between the surface of electrode and electrolyte but also the concentration of the electrode and electrolyte materials itself. *Ohmic losses* are referred as the resistive losses taking place in the electrodes due to Ohm's law ($U = IR$) [16]. Polarization losses are particularly dependent on the battery charge and SOC while ohmic losses changes as the battery ages and chemical structures perishes permanently which are affecting to the SOH. Moreover the internal impedance of the battery provides information that could be used for both SOC and SOH estimation. [4, 5]

3.3 Lithium-ion Batteries

Lithium's features as the lightest metal available among the chemical elements, high electrode potential and high energy density makes it optimal compound to be used in batteries. Over the years, two major approaches are proposed as lithium battery technology. first design is so-called lithium-metal batteries in which the lithium metal is used as the active-material at negative electrode. However, pure lithium's high reactivity makes it unstable material to be used in secondary batteries charge. In the second design, lithium is used as ions (Li^+) in the electrolyte and also in both electrodes lithium-ion making it far more stable compound in cycle use. Safety issues makes lithium-ion technology predominant over the lithium-metal technology in secondary batteries. [16, 20]

Different lithium-ion battery technologies are i.e. lithium cobalt oxide ($LiCoO_2$), lithium iron phosphate ($LiFePO_4$) and lithium-ion manganese oxide ($LiMn_2O_4$). The name of the technology basically refers to the material used as positive electrode in the battery. Metal required at negative electrode to complete redox process is usually graphite (C_6). Electrolyte is usually some kind of salt compound (i.e. lithium hexafluophosphate salt ($LiPF_6$)) which is effective ion conductor. Battery

technology have significant effect on the terminal voltage and energy density of the battery. Some of the most common lithium-ion technologies are listed and characterized in table 3.1.

Acronym	Positive electrode	Negative electrode	Cell voltage (V)	Energy density ($\frac{Wh}{kg}$)
LCO	$LiCoO_2$	Graphite	$3.7 - 3.9$	140
NMC	$LiNiMnCoO_2$	Graphite	$3.8 - 4.0$	170
LMO	$LiMn_2O_4$	Graphite	4.0	120
LFP	$LiFePO_4$	Graphite	$2.3 - 2.5$	100

Table 3.1 *The most popular lithium-ion technologies developed so far [20]*

Still at the moment, graphite is the predominant compound within all technologies at negative electrode. However, it should be mentioned that lithium-titanate-oxide $Li_4Ti_5O_{12}$ at the negative electrode has started to gain popularity since capacity improvements in terms of positive electrodes has more or less reached their limits. In terms of positive electrode technologies, $LiFePO_4$ has the lowest terminal voltage and energy density compared to other technologies but it also is the most stable and safe technology. $LiCoO_2$ is very popular at the moment especially in the portable applications due to high energy density. However, it's short life-cycle, low thermal stability, restrictions on charge and discharge current and high price of the cobalt will move the trend away from this technology in the future. It is also relatively rare material and will run out in the future as battery applications drastically increases. $LiMn_2O_4$ batteries can be charged and discharged with heavy current due to low internal impedance. This feature makes it candidate in the electric vehicle applications. In reality, $LiMn_2O_4$ is rarely used because of the poor capacity. $LiNiMnCoO_2$ is at the moment the most promising technology in the field of automotive and ESS industry. It has high cell voltage and energy density but it also has been develop to unite the pros of the each sub-element (manganese, nickel and cobalt). [18, 20]

Also lithium-ion technologies are based on redox process. When considering $LiCoO_2$ technology, the two half-cell reactions can be presented as follows.

Positive electrode:

$$\mathrm{LiCoO_2} \underset{\text{charge}}{\overset{\text{discharge}}{\rightleftharpoons}} \mathrm{CoO_2}^{+}\,\mathrm{Li}^{+} + \mathrm{e}^{-} \tag{3.4}$$

Negative electrode:

$$\mathrm{C_6} + \mathrm{Li}^{+} + \mathrm{e}^{-} \underset{\text{charge}}{\overset{\text{discharge}}{\rightleftharpoons}} \mathrm{LiC_6} \tag{3.5}$$

When summing equations together and eliminating electrons and lithium ions, we get following overall reaction.

$$\mathrm{LiCoO_2 + C_6} \underset{\text{charge}}{\overset{\text{discharge}}{\rightleftharpoons}} \mathrm{CoO_2 + LiC_6} \tag{3.6}$$

Electrolyte in Lithium-Ion batteries is only conducting lithium-ions between the electrodes and not taking part to the redox process. This results the internal impedance of the lithium-ion battery to remain approximately constant until the end of discharge where polarization of the electrodes increases the internal impedance. This makes the estimation of SOC more difficult than with lead-acid batteries in which electrolyte is also taking part to the redox process which changes the internal impedance in a more linear manner [16]. However, internal impedance is still an informative characteristic in Lithium-ion batteries as is later shown in this thesis.

One of the greatest drawbacks of lithium-ion batteries is their inability to withstand over-discharging and overcharging. Over-discharge can make the battery to *sleep* which means it does not respond to charging. This basically makes the battery useless even though some batteries can be revived back to life with boosted charging. This is usually avoided by defining a cut-off voltage for the battery. Overcharge can lead temperature rise and unstable operation (thermal runaway). Thus requirements for BMS in lithium-ion batteries are more restricted than in many other battery technologies. To prevent overcharge, constant current - constant voltage (CC-CV) charging algorithm is often used. When connected to a charger, battery is charged with a constant current until the voltage rises to a certain threshold. Charge current is then decreased in a way that voltage remains constant. When current is decreased below a certain threshold, battery is considered to be fully charged. A float charging is then often applied to maintain certain OCV which would otherwise slowly decrease due to self-discharging of battery. [16, 18, 20]

3.4 Battery modeling

To be able to realistically simulate and predict the state of a battery, quantities and phenomenons in batteries should be modeled mathematically with a relations that would eventually describe the real operation of a battery as accurately as possible. Simple models are often inaccurate but computationally light whereas more complex multi-variable models are more accurate but computationally heavy. Modeling is thus often a compromise of these two and some assumption are always made so the models never describes the reality perfectly. Battery models in literature often

focuses on one or two quantities to be modeled accurately at least at a time. In terms of this thesis, particularly battery voltage and internal impedance are on the main focus relevant models for these quantities are introduced below.

3.4.1 Linear model

Probably the simplest model of the battery is achieved by modeling the internal impedance with a pure resistance in series with an ideal voltage source. Such model is illustrated in figure 3.2.

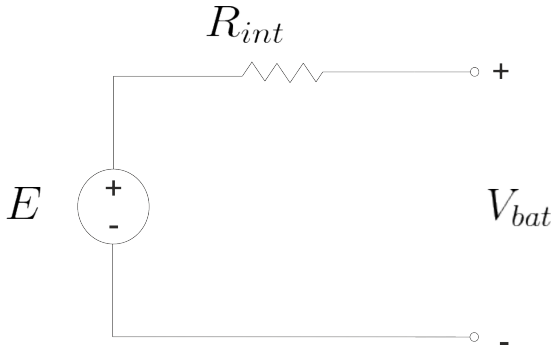

Figure 3.2 *Equivalent circuit diagram of a linear battery model*

In the model in figure 3.2, V_{bat} is determined only by the current in the circuit that causes a voltage drop over the internal resistance R_{int} since ideal source voltage E is presumed constant. Linear model in the form that is presented above gives quite poor approximation for the terminal voltage V_{bat} because quantities like SOC, SOH and temperature are neglected. However, a huge improvement can be made if E and R_{int} is dependent on the SOC. [21, 22]

3.4.2 Randles' model

Better approximation than in figure 3.2 for the internal impedance can be achieved if also the polarization losses are separately modeled. Such circuit in it's conventional form is illustrated in figure 3.3.

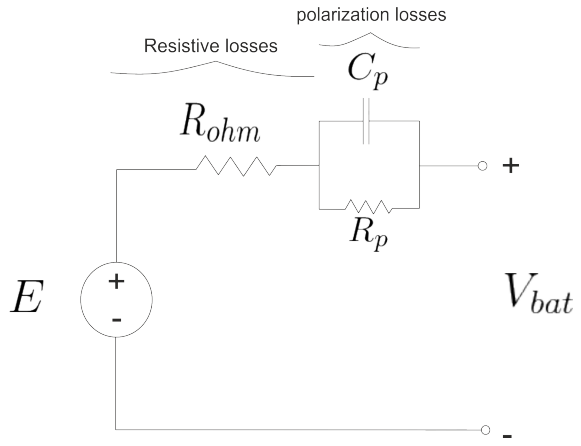

Figure 3.3 *Equivalent circuit diagram of Randle's circuit model*

Circuit in figure 3.3 is also known as Randle's model (or circuit) first introduced by J.E.B. Randles [23]. Usefulness of the Randles' model lies on the feature that it's parameters can be defined graphically from the complex impedance spectrum. Conventional form of the circuit is often modified by inserting series connected RC-branches or other inductive- and constant-phase elements to better parametrize the different regions from complex impedance plots. [24–26]

3.4.3 A controlled voltage source battery model

Two previously introduced models are models that are based on the internal impedance models. This means that source voltage is assumed to remain constant and battery terminal voltage is only determined by internal impedance and current. Model introduced in this section is basically the linear model already introduced above but with a controlled voltage source [22,27–29]. Source voltage is changing as a function of battery charge according to the following equation

$$V_{bat} = E - R_{int} I_{bat}, \tag{3.7}$$

where E is the battery source voltage which is defined as follows.

$$E = E_0 - K\frac{Q_0}{Q_0 - Q} + Ae^{-BQ} \tag{3.8}$$

All variables in (3.7) and (3.8) are defined in table 3.2.

V_{bat}	Battery terminal voltage (Ah)
E	Battery source voltage (V)
E_0	Battery constant voltage (V)
K	polarization constant (V/Ah)
Q	consumed charge from the battery (Ah)
Q_0	Rated battery capacity (Ah)
A	Exponential zone amplitude (V)
B	Exponential zone time constant inverse (Ah^{-1})
I_{bat}	Battery current (Ah)
R_{int}	Battery internal resistance (Ah)

Table 3.2 *Variable description of the generic battery model*

Q is defined to be zero when the battery is fully charged since no electric charge has been transferred from the battery. Q is obtained by integrating the battery current due to the well known equation.

$$Q = \int_0^t -I_{bat} dt = -I_{bat} t \tag{3.9}$$

Notable is the negative sign of I_{bat} since positive direction of the current is chosen away from (discharging) and negative direction towards the battery. Whole model described above can be illustrated as equivalent circuit model presented in figure 3.4.

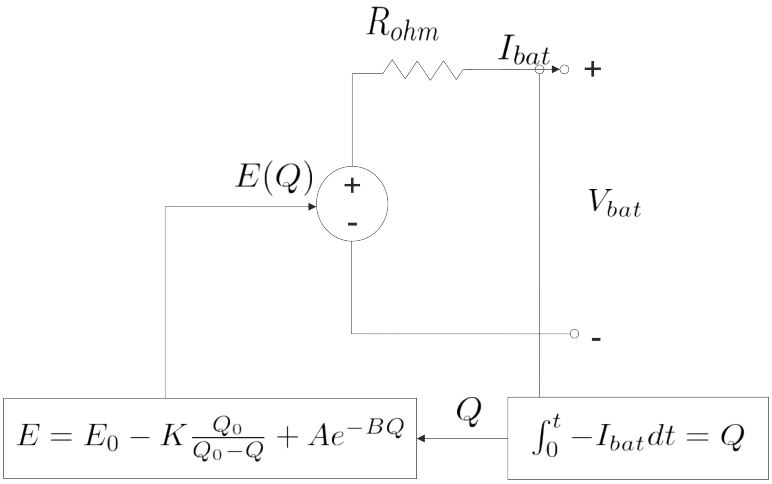

Figure 3.4 *Equivalent circuit diagram of a generic battery model with controlled voltage source*

Similar to Randles' model, also parameters in this model can be graphically defined by using the look-up tables from the battery datasheet. Usually internal resistance R_{int} and rated capacity Q_0 are given as values in datasheets. Rest of the variables

can be extracted from the V-Q curve look-up table similar to one in figure 3.5.

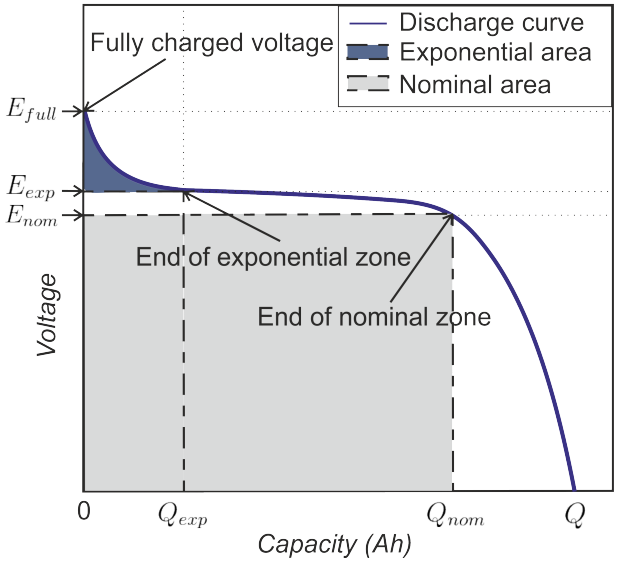

Figure 3.5 *Principal look-up table of a battery during discharge [27]*

Three important regions presented in the figure 3.5 are *fully charged voltage*, *end of exponential zone* and *end of nominal zone*. When neglecting the internal resistance, i.e. considering only the source voltage equation (3.8), exponential zone amplitude A can be derived as follows.

$$A = E_{full} - E_{exp} \tag{3.10}$$

In equation (3.10) E_{full} is the battery source voltage at fully charged point and E_{exp} is the battery source voltage at the end of exponential zone. Thus A can be graphically derived from figure 3.5. For B, we can use also the information available at the end of exponential zone. Exponent function has settled to almost zero (5%) after three time constants. By using this information, we get

$$BQ_{exp} = 3 \qquad \Longleftrightarrow \qquad B = \frac{3}{Q_{exp}} \tag{3.11}$$

Also the actual charge at the end of exponential zone Q_{exp} can be obtained from the look-up table as previously mentioned. Two other unknowns E_0 and K can be solved by forming a pair of equations for the source voltage at the point of fully charged voltage (3.12) and at the end of nominal zone (3.13).

$$E_{full} = E_0 - K + A. \tag{3.12}$$

$$E_{nom} = E_0 - K\frac{Q_0}{Q_0 - Q_{nom}} + Ae^{-BQ_{nom}} \tag{3.13}$$

At fully charged point, $Q = 0Ah$ and equation (3.8) reduces to equation (3.12). There are now two equations with two unknowns and thus E_0 and K can be solved by first eliminating and substituting either unknown to either equation. For instance, when solving K from (3.12) and substituting it to (3.13), we get the following for E_0.

$$\begin{aligned} E_0 &= E_{nom} + (E_0 - E_{full} + A)\frac{Q_0}{Q_0 - Q_{nom}} - Ae^{-BQ_{nom}} \\ \iff E_0(1 - \frac{Q_0}{Q_0 - Q_{nom}}) &= E_{nom} + (-E_{full} + A)\frac{Q_0}{Q_0 - Q_{nom}} - Ae^{-BQ_{nom}} \\ \iff E_0 &= \frac{E_{nom} + (-E_{full} + A)\frac{Q_0}{Q_0 - Q_{nom}} - Ae^{-BQ_{nom}}}{(1 - \frac{Q_0}{Q_0 - Q_{nom}})} \end{aligned} \tag{3.14}$$

Now all the parameters in(3.8) are known. Internal resistance could also be added to the equation (just like in(3.7)) since R_{int} can be obtained from the battery datasheet and I_{bat} is the function variable for the model.

However, when modelling battery in a way described above, some assumptions need to be made. These assumptions are:

- *Internal resistance* is assumed to be constant and not affected by I_{bat}.
- *Battery capacity* is assumed to be constant and independent on I_{bat}. (Peukert's effect not included)
- *Temperature* dependency is not included.
- *Self-discharge* is not taken into account.

In reality, statements above are invalid and are clearly affecting to the validity of the

model. However, since batteries are highly nonlinear systems, some assumptions are always needed to be made. This model also trusts the validity of the look-up tables and variable values given in datasheets which in reality are suggestive and changes as the battery ages.

3.4.4 Discussion of the models

As was already stated, linear model as it is in figure 3.2 is highly inaccurate model of a battery since all the quantities (battery voltage and resistance) it models are assumed to be constant. However, it is the equivalent circuit that all the models are based on and is thus mentioned here.

Randles' model is a better approximation for the battery internal impedance. On the other hand, the controlled voltage source battery model is better approximation for battery terminal voltage as a function of battery charge and SOC. This is important feature when simulating operation of BESS in renewable energy application which is in the focus of this thesis. The best solution would, of course, be union of these two models which is applied further in this thesis. However, in this thesis battery impedance is not measured to find the parameters for the Randles' model unlike in many other published papers. Instead, measured frequency response data is fitted to a transfer function that models the internal impedance regardless of how it can be parametrized. Such combination of controlled voltage source model and Randles' model is thus further used in this thesis.

4. BATTERY INTERNAL IMPEDANCE MEASUREMENT TECHNIQUES

Internal impedance is always tight together with battery itself and it cannot be realized apart. This introduces difficulties to it's measurements that must be carried out concentrating on the changes in measured quantities that are terminal voltage and current of the battery. These changes must be applied to the system in a way that is somewhat known which gives rise to a need of excitation signal. Impedance has different response at different frequencies which means that results should be analyzed in complex form or in frequency domain.

4.1 System identification

A linear time-invariant (LTI) system with input signal $x(t)$ and output signal $y(t)$ can be characterized by a system impulse response $g(t)$ or transfer function $G(j\omega)$ as follows [30].

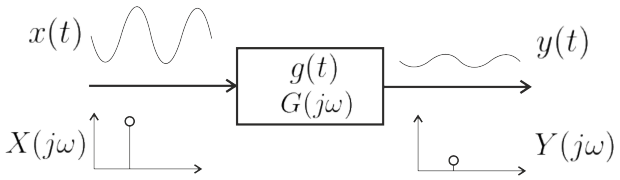

Figure 4.1 *Block diagram of a linear time-invariant system*

Uppercase vectors are complex vectors that are represented in frequency domain and are Fourier transforms of the lowercase letter time-domain signals. Frequency content of a time-domain signal (lowercase letters in figure 4.1) can be extracted by applying Fourier-transform to time-domain signals which is mathematically expressed below in continuous form.

$$G(j\omega) = \int_{-\infty}^{\infty} g(t)e^{-j\omega t}dt \tag{4.1}$$

However, a discrete fourier transform (DFT) is often used since digital systems cannot cope with continuous signals. A modified algorithm called fast fourier transform (FFT) is further used to calculations in this thesis since it reduces the computational burden introduced by normal DFT [30]. LTI system in figure 4.1 can be mathematically expressed as

$$Y(j\omega) = G(j\omega)X(j\omega) \quad \Leftrightarrow \quad G(j\omega) = \frac{Y(j\omega)}{X(j\omega)}, \tag{4.2}$$

where Y is the output, X is the input and G is the system frequency response function. When considering Ohm's law

$$U(j\omega) = Z(j\omega)I(j\omega) \quad \Leftrightarrow \quad Z(j\omega) = \frac{U(j\omega)}{I(j\omega)}, \tag{4.3}$$

similarities to (4.2) can be easily seen. Current is the input of the system, voltage is the output and impedance is the system transfer function. Such representation is quite useful considering battery impedance measurements because of the battery internal impedance's varying response to different frequencies which is later shown in this thesis.

4.2 Excitation signals

Straight measurements from the input and output in (4.3) during charging and discharging gives no information about the internal impedance. Instead, by perturbing the battery with an excitation signal and measuring the changes in current and voltage, information can be achieved. However, different excitation signals have different impact on the results. To extract the desired content of the system, excitation signal needs to be carefully designed. Principal block diagram of a excited system is shown in figure 4.2,

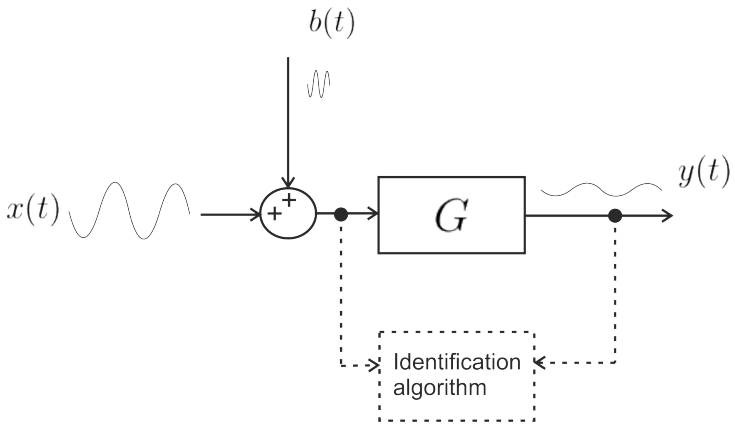

Figure 4.2 *System frequency response measurement with the use of excitation signal*

where $x(t)$ is the input and $y(t)$ output of the system. The place of the excitation $b(t)$ injection depends highly on the application. Considering the fact that battery is realized as voltage source, battery current is the quantity that should be perturbed and thus perturbation is located at the input side in figure 4.2.

4.2.1 Sine sweep

In sine sweep method, perturbation is a sine wave with only the fundamental frequency as frequency content. In mathematical form this is

$$x(t) = Asin(2\pi ft). \tag{4.4}$$

Sine sweep has quite high Signal to Noise Ratio (SNR) which is due to the fact that only one frequency is swept at a time. SNR can also be increased up to a certain point by increasing the amplitude A of the excitation. It is also suitable for analysis of non-linear systems since it's harmonic content is directly visible [30]. Significant drawback however is that each frequency has to be injected separately which increases the measurement time. Sine wave is also difficult heavy to implement digitally since it has characteristics of continuous signal and a lot of bits are required to represent an accurate discrete estimate. Sine is widely used in EIS measurements which is widely used method for battery impedance characterization [24–26]. However, measurements carried out in this thesis are different from EIS since measurements are applied during discharge of the battery with nonzero DC-current while conventional EIS measurements are carried out with zero DC-current. This was due to the lack of suitable equipment in the laboratory that would allow bi-directional powerflow between the DC-load and the battery.

4.2.2 Pseudo random binary sequence (PRBS)

PRBS is a broadband excitation signal since that contains energy at several frequencies. It is a binary signal which has only two levels. PRBS is often used in a form of maximum length binary sequence (MLBS) in which the sequence is realized with $N = 2^n - 1$ samples n being the number of registers used for generating the sequence. MLBS form of PRBS is also used in this thesis but only term PRBS is used in further section to avoid confusion. Example of a 3-bit PRBS is shown in figure 4.3

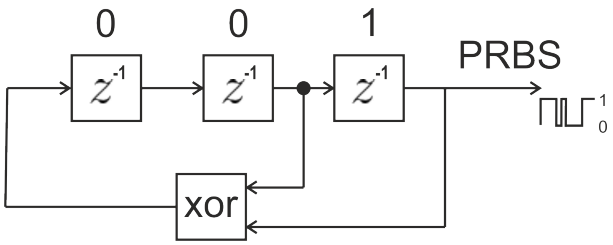

Figure 4.3 *Block diagram of a 3-bit PRBS*

Boxes with z^{-1} in them represents shift registers that acts as a unit delay in which one's input is shifted to it's output within one generating interval. This is determined by the generating frequency f_{gen} of the PRBS. PRBS should also be sampled at higher frequency rate than f_{gen} to avoid aliasing. According to well known sampling theorem, sampling frequency f_s should be at least twice the highest frequency of interest.

Sequence is created by setting initial condition for the shift registers. can be any combination except the state [000]. All other combination can be used as initial condition and are repeated once during one sequence that now has $N = 2^3 - 1 = 7$ different states. Exclusive-or gate (Xor) is then used to make the sequence to continue and repeat. It's position is however of great importance and it cannot be set between any arbitrary registers. Possible feedback routes from shift registers are presented in [30].

According to [31], Power of the PRBS is given as

$$\Phi_{PRBS} = a^2 \frac{(N+1)}{N} \frac{sin^2(\pi q/N)}{(\pi q/N)^2}, \quad q = \pm 1, \pm 2, ... \tag{4.5}$$

where a is the amplitude of PRBS, N is the length of the sequence in samples and

q is the sequence number that determines the corresponding frequency due to the relation $f_q = qf_{res}$. f_{res} is the frequency resolution of the PRBS which is determined by f_{gen} and N as follows

$$f_{res} = \frac{f_{gen}}{N}, . \tag{4.6}$$

f_{res} is also the lowest frequency that the PRBS has energy at. Power spectrum of a PRBS obtained with (4.5) is shown in figure 4.4.

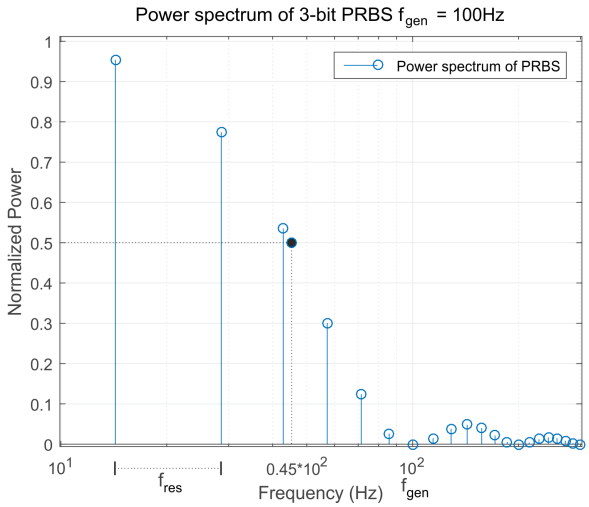

Figure 4.4 *Power spectrum of 3-bit PRBS*

It can be seen that power reduces as the frequency increases being zero at f_{gen}. Beyond that frequency, the spectrum is mirrored with reduced power. In reality, this means that reliable information cannot be acquired at frequencies close to f_{gen} and beyond. Relatively reliable frequency band is often regarded as $\approx 0.45 f_{gen}$ since the power is reduced to half at that frequency. This is also illustrated in figure 4.4.

Due to the broadband behavior of PRBS, measurement time can be significantly reduced compared to sine sweep. Having the same frequency resolution, PRBS measures all the corresponding frequency points in a time equal to $T_{meas} = \frac{1}{f_{res}}$ while sine sweep has measured only one. This reduced time can be thus used for averaging several consecutive periods of PRBS. With M periods to average, SNR can be increased by a factor $\sqrt{M}$. By using averaging, the amplitude of the perturbation can be kept very low which is extremely useful when measuring sensitive systems. [31]

Besides the speed of PRBS, one very desired characteristic is also it's binary form

which makes it easy to be generated and implemented implemented digitally to a system in real applications. Square wave perturbation is already used in MPPT algorithms [14] through DC-DC converter duty ratio. It is also discussed in [32, 33] that square wave sweep can be used in the same way for battery internal impedance measurements. PRBS measurements are also implemented in [6–8] but so far with specifically designed laboratory environment though it certainly has indisputable potential for commercialized products.

4.3 Battery internal impedance measurements

Battery measurements are implemented here using both sine sweep and PRBS excitation signals. Impedance is measured from one commercialized Lithium-Ion battery (36V, 2.6Ah). Results obtained for Lithium-Ion battery are further used in simulations in section 6.

4.3.1 Laboratory setup

Principal measurement scheme is shown in figure 4.5.

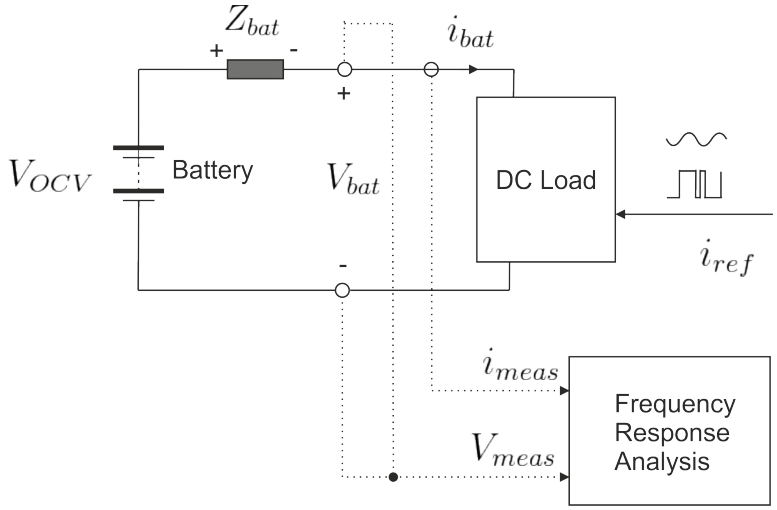

Figure 4.5 *Principal scheme of the battery impedance measurement setup*

In figure 4.5 V_{OCV} is the battery open-circuit voltage, Z_{bat} is the internal impedance of the battery and V_{bat} is the voltage between battery terminals which is different to V_{OCV} when battery draws any current. Excitation signals are perturbed into the circuit as current reference i_{ref} to the DC-load device that draws a current which is the same as battery current i_{bat}. Current and terminal voltage of the battery are

measured (i_{meas} and V_{meas}) with high-resolution current- and voltage probes and calculations are made with computer. Measurements are only carried out by means of discharge of the battery which is due to the characteristics of DC-load device that can only absorb power.

Laboratory setup used for measurements is shown in figure 4.6.

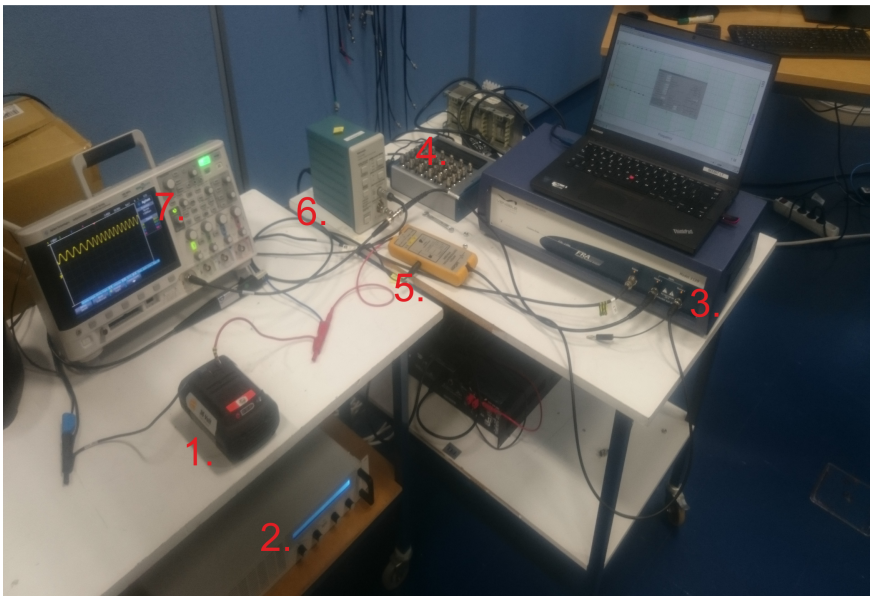

Figure 4.6 *Laboratory setup of the battery impedance measurements*

Numerated devices in figure 4.6 are explained as follows.

1. Lithium-Ion battery pack (36V, 2.6Ah)
2. DC-load used for discharge of the battery and as a link to the perturbation signals
3. Venable frequency response analyzer used for creating the excitation signal and for data acquisition during sine sweep measurements
4. NI USB-6363 DAQ device used for creating the excitation signal and for data acquisition during PRBS measurements
5. Voltage probe
6. Current probe
7. Oscilloscope for visualizing the measurements and excitation signals

After each measurement instant, battery was discharged with constant current for 1 minute with PRBS and 1-2 minutes with Venable before starting new measurement. Rough window with Venable measurements was due to the fact that each measurement was to start manually. SOC of the battery was monitored actively throughout the measurements by using *Coulomb counting*.

4.3.2 Optimizing parameters for excitation signals

Measurement parameters for sine-sweep measurements are shown in table 4.1.

	Sine sweep	PRBS
Offset	$1A$	$1A$
Amplitude	$0,25A$	$0,25A$
Averaging	10 cycles	10 cycles
frequency range	$100mHz - 5kHz$	$100mHz - 5kHz$
f_{gen}	-	$204.7Hz$ and $15kHz$
f_s	-	$8 * f_{gen}$
n	-	11 and 14
Measurement time	$500s$	$120s$

Table 4.1 *Parameters for measurements*

Due to the characteristics of the DC-load used for measurements, perturbations are formed with offset that will ensure the discharge operation. Current should not go to zero since temporary open-circuit conditions will affect to the measurements. DC discharge current was chosen to equal 1A which was considered as a good compromise that might not affect to the battery capacity significantly. In reality, battery capacity will fade when higher current is applied. On the other hand, too low current would not affect to battery terminal voltage that much and voltage measurement would suffer from increased SNR. Also the perturbation amplitude was chosen to equal 0.25A which was empirically tested to give satisfying results. In reality, this would be too large perturbation since it is 25% of the DC-current but the purpose here is just verify that PRBS could be used for measurements and this is further discussed in the section 4.5.

Frequency range was determined as 100mHz - 5kHz which affects to the design of PRBS. Lowest frequency will determine the frequency resolution. PRBS should also reliably cover the frequencies up to 5kHz which means that generating frequency must be over 2-times higher since only $0.45f_{gen}$ are considered to be reliable. PRBS with frequency resolution of at least 100mHz and generating frequency of 15kHz will have $N = \frac{f_{gen}}{f_{res}} = \frac{15000Hz}{0.1Hz} = 150000$ samples means that at least 18-bit register should

be used. Yet this not a problem in practice but such a long PRBS was found to affect to the results by introducing significant offset especially at lower frequencies. This is unacceptable since interesting phenomena will appear at lower frequencies. This is why PRBS was eventually perturbed by using two different sequences one concentrating on lower frequencies and one on higher. Obtained results are then united to form a desired frequency band.

The use of two separate PRBS signals increases the total measurement time. Ideally it would be the same as $\frac{1}{f_{res}} *$averaged periods $= \frac{1}{0.1Hz} * 10 = 100s$ but the other high-frequency PRBS with frequency resolution of 1Hz increases this time. In reality the measurement time is slightly lower because DAQ is initialized in the beginning of every measurement which takes several seconds. 2 minutes is quite a long time for measurements but this is the price that needs to be payed if low frequencies are of interest. Measurement time is still significantly lower with PRBS than with sine sweep.

4.4 Measurement results

Measurement results for sine sweep and PRBS measurements as 2-D figures with five different SOC values and 3-D figure for all measurements are shown in figures 4.7 - 4.10. Finally the measurements with both methods at individual SOC are shown in figures 4.11 - 4.15.

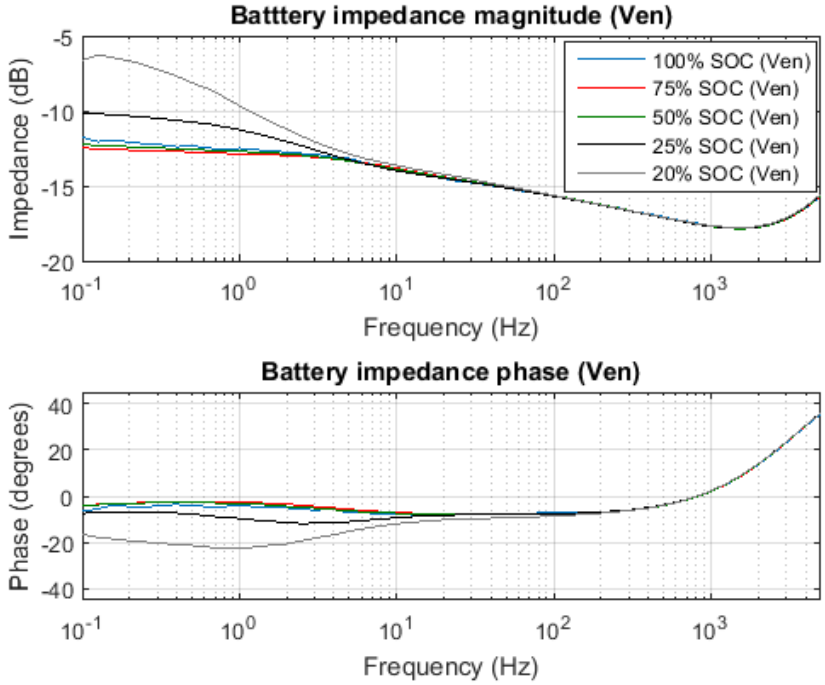

Figure 4.7 *Sine sweep measurements of battery internal impedance with 5 different SOC*

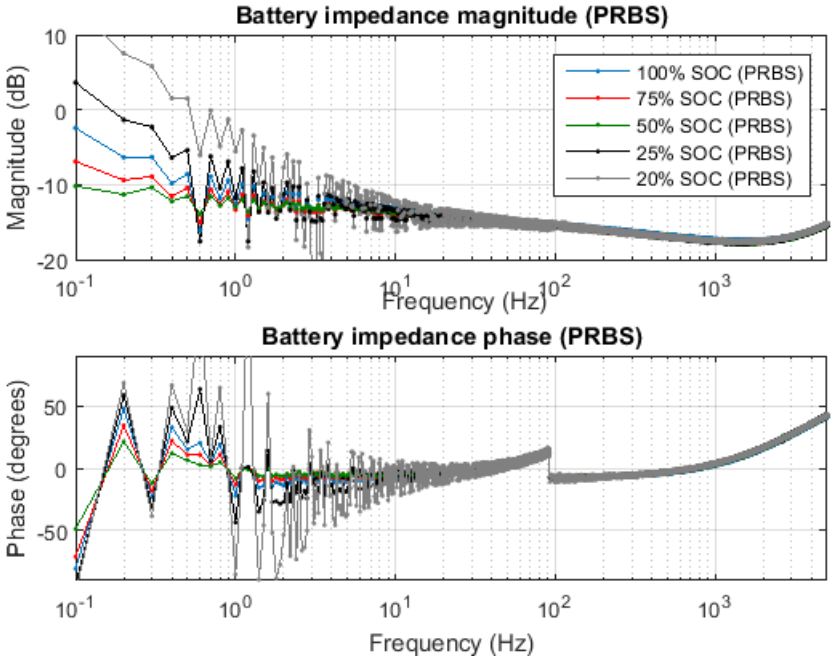

Figure 4.8 *PRBS measurements of battery internal impedance with 5 different SOC*

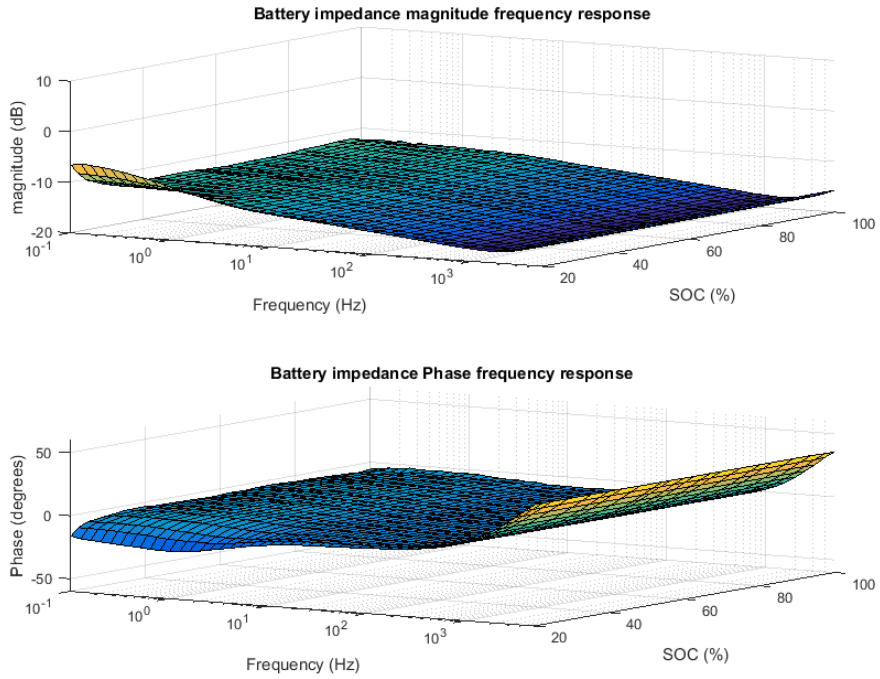

Figure 4.9 *Sine sweep measurements of battery impedance as a function of frequency and SOC*

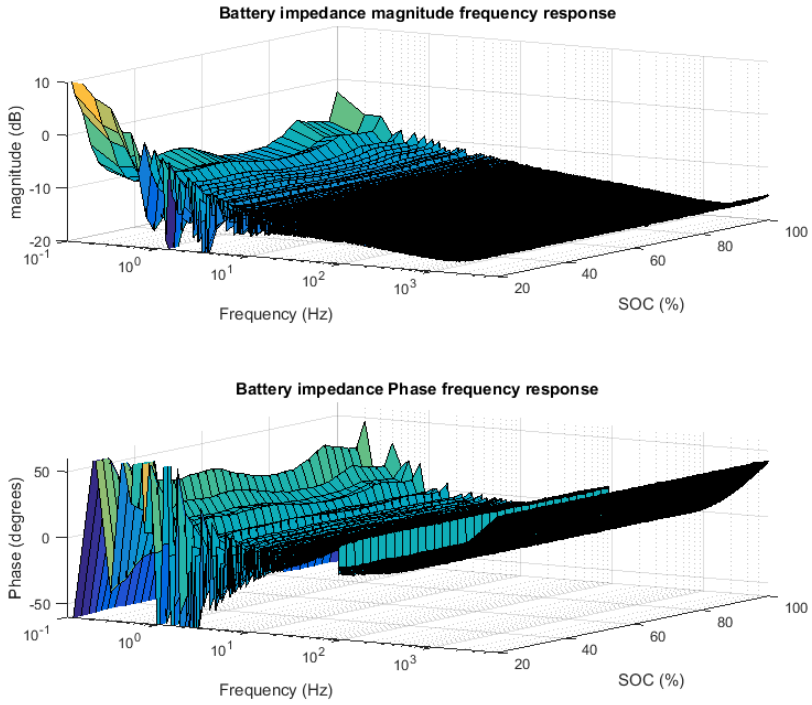

Figure 4.10 *PRBS measurements of battery impedance as a function of frequency and SOC*

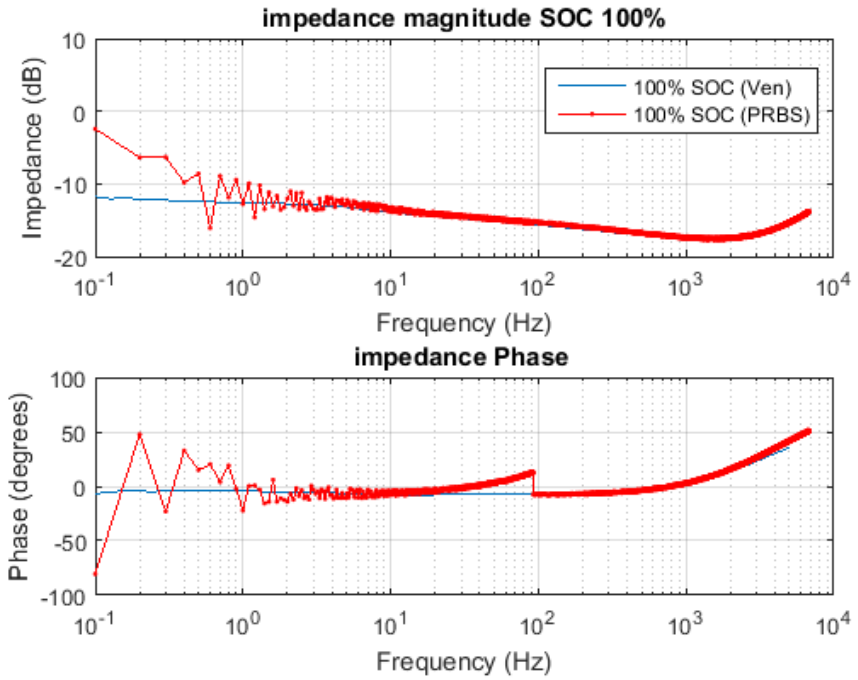

Figure 4.11 *PRBS and sine sweep measurements with SOC = 100%*

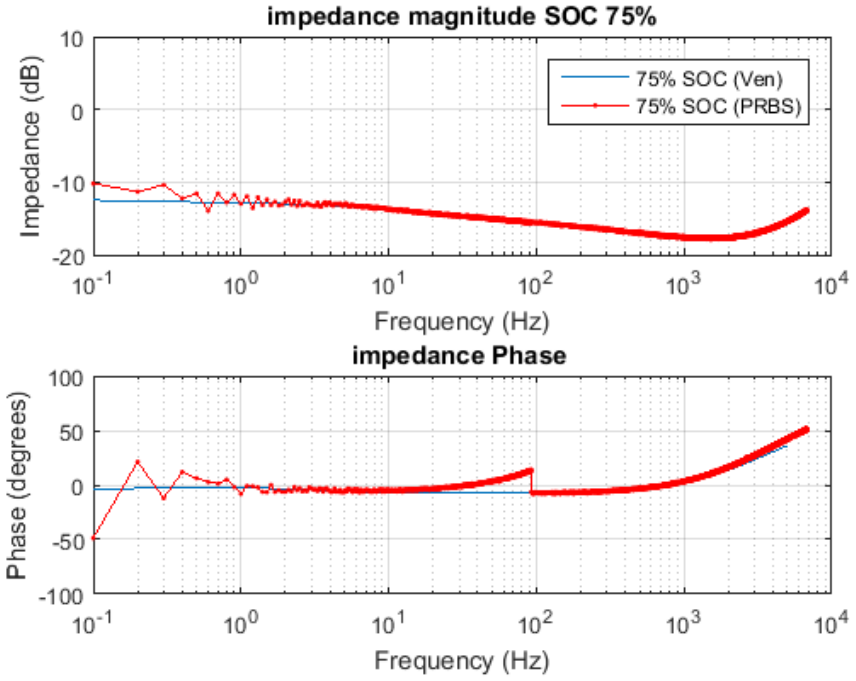

Figure 4.12 *PRBS and sine sweep measurements with SOC = 75%*

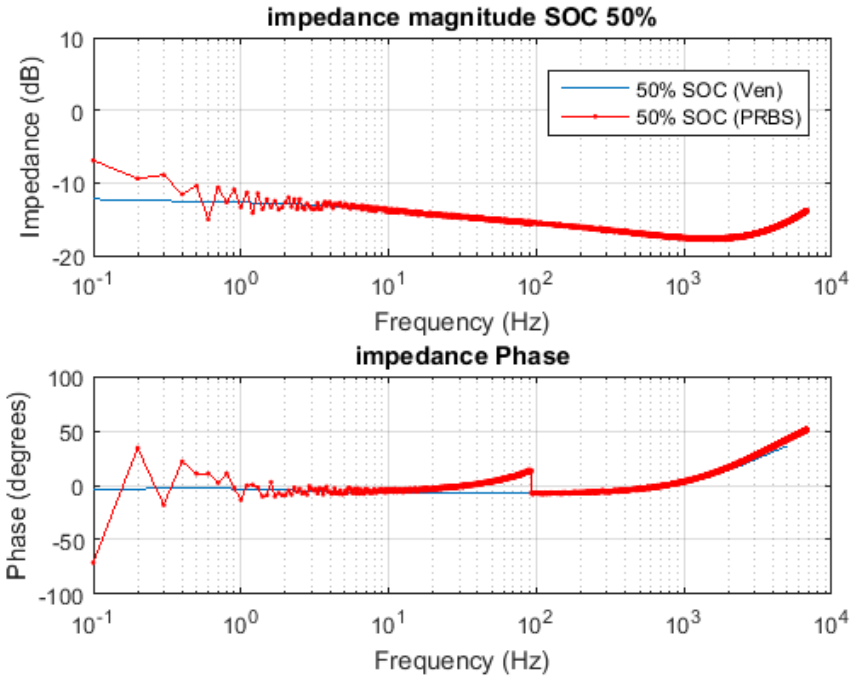

Figure 4.13 *PRBS and sine sweep measurements with SOC = 50%*

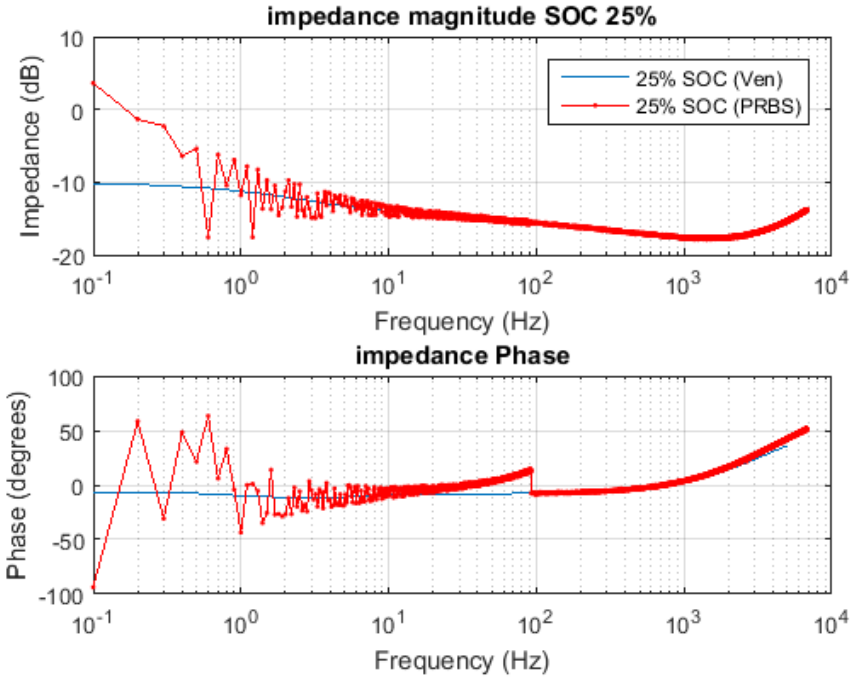

Figure 4.14 *PRBS and sine sweep measurements with SOC = 25%*

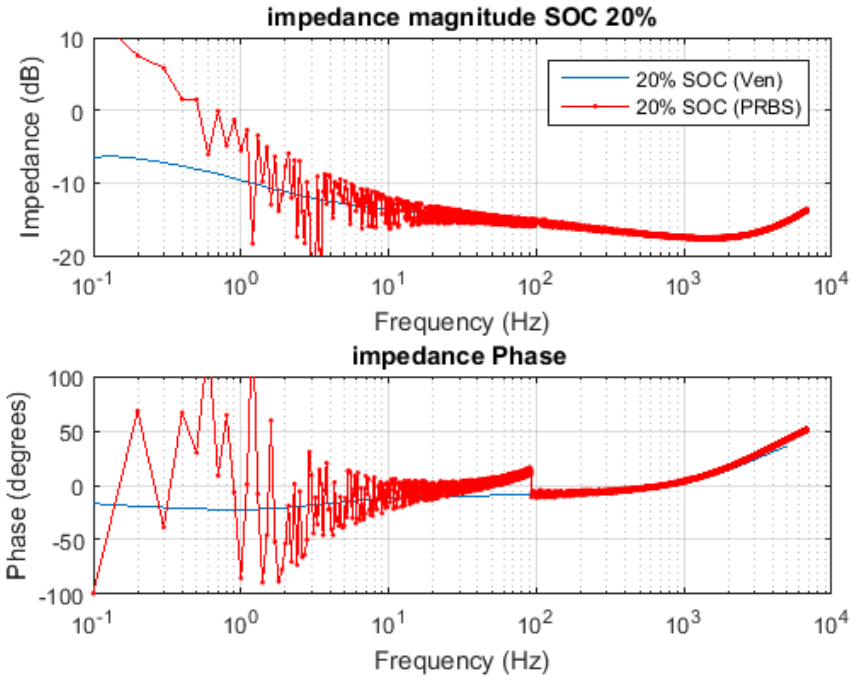

Figure 4.15 *PRBS and sine sweep measurements with SOC = 20%*

4.5 Analysing the Results

By first discussing the resemblance between the two measurement methods, it can be seen that both excitation signals give roughly similar results for battery impedance. Especially frequencies from 10Hz up to 5kHz are matching well. This frequency region is important especially for SOH estimation. Nevertheless there are huge distortion involved to the PRBS results. There are both offset and relatively high deviation affected to the results especially at frequencies below 10Hz in all above figures. These aspects could not be mitigated by changing parameters presented in table 4.1. Phase response is also affected by a point of irregularity which is due to the use of two separate PRBS sequences. Phase acts similarly to Venable measurements in the high-frequency PRBS but the low-frequency PRBS experiences linearly raising trend in the phase. It was concluded that this is due to the used DAQ device but it was not succesfully compensated from the results. Noteworthy is also the trend between adjacent frequency points in figure 4.8. If one datapoint has lower magnitude than the previous and vice versa, it will be the case in all measurements which refers to a conclusion that phenomenon is due to the nonlinear battery characteristics. It is stated [18] that battery is a non-linear device and this non-linear behaviour is also present in it's internal impedance. It is stated that PRBS should be used for linear systems and sequence itself should be modified to better deal with non-linear systems [30] but it do provide accurate results for almost full frequency band that was measured.

It can be seen that impedance is increased at low frequencies as the SOC decreases to 25% and less. No significant changes are visible at higher frequencies. Also the impedance tends to be slightly higher at full charge (100%) than at 75% . Trend is more harsh and visible in the PRBS measurements though the results are highly distorted. Measurements with PRBS can thus provide quite good relative approximate of the impedance even though its absolute value and frequency response is hard to obtain. Therefore the results obtained with sine-sweep and Venable are further used in this thesis to simulate the battery impedance load- and source effect.

4.6 Estimation of linear transfer function from the measurement results

To further use the measured data in the Simulink environment, a linear estimate of the measurement data should be derived that can be presented as linear transfer function in Laplace-domain. Instead of deriving parameters for the Randles' impedance model presented in section 3.4.2, *tfest* -function is used in MATLAB

to provide relatively accurate linear estimate for the battery impedance. Empirical inquiries resulted that 4th-order estimate gives the best estimate. Estimates are derived for measured impedances at 75% (lowest impedance at low frequencies) and 20% (highest impedance at low frequencies). Following transfer function are obtained.

$$Z_{SOC-75\%} = 10\frac{45.6903s^4 + 3.1495e5s^3 + 9.9232e7s^2 + 1.3615e9s + 1.7083e8}{s^4 + 2.3768e6s^3 + 5.6879e8s^2 + 6.0252e9s + 6.7119e8} \quad (4.7)$$

$$Z_{SOC-20\%} = 10\frac{2.8162e3s^4 + 2.0897e7s^3 + 1.9479e9^2 + 3.3337e9s + 1.3017e8}{s^4 + 1.5267e8s^3 + 9.2687e9s^2 + 7.1518e9s + 6.7514e7} \quad (4.8)$$

In above transfer functions s denotes the Laplace-variable. Impedances are obtained for the 36V Lithium-ion battery pack which most likely has 10 series-connected cells inside (no datasheet available because battery pack is included with commercial leisure time tool). Battery pack voltage for the simulations was set to 360V (as later stated in section 6) which is obtained when connecting ten 36V battery packs in series if there is no cells connected in parallel. Transfer functions in 4.7 and 4.8 must therefore be multiplied by a factor 10 as is marked. This is very harsh approximation and most likely would not be relevant in reality. Battery packs usually have also parallel connected strings that would decrease the internal impedance of the whole battery pack. Relevancy is further discussed in section 7. Estimates with and without multiplication are illustrated in figures 4.16 and 4.17 and estimated impedances in Laplace-domain are further taken into account in battery charger dynamics analysis in section 5.4.

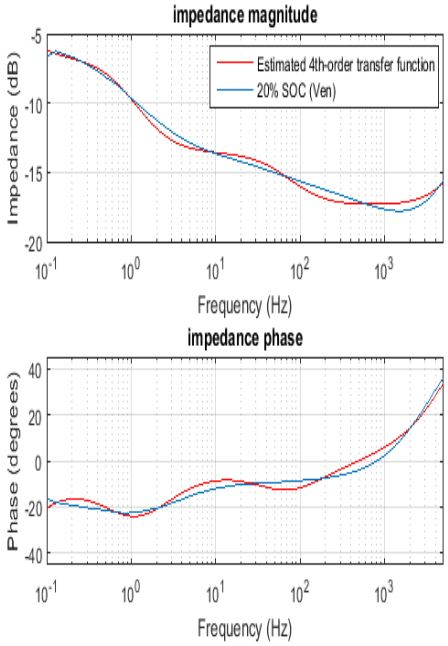

((a)) $SOC = 20\%$

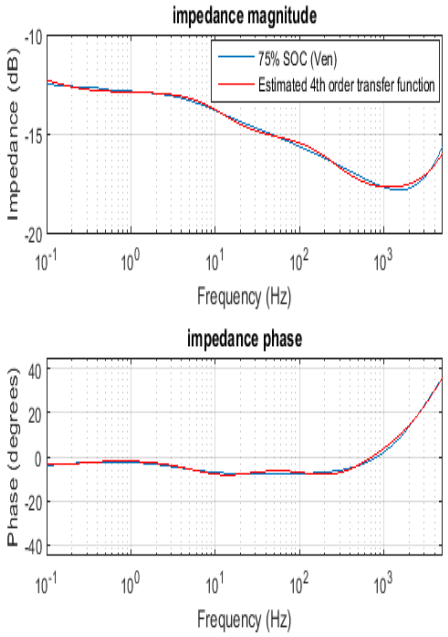

((b)) $SOC = 75\%$

Figure 4.16 *Measured and 4th-order estimated battery impedances*

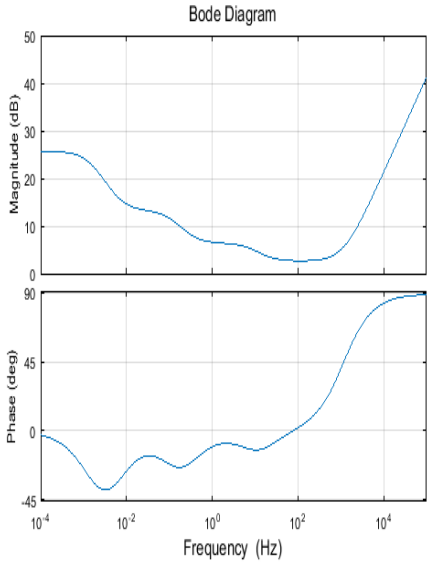

((a)) $SOC = 20\%$

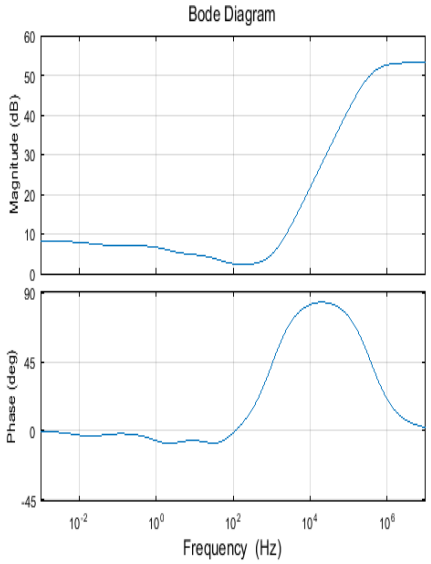

((b)) $SOC = 75\%$

Figure 4.17 *Estimated battery impedances multiplied by 10*

5. DC-DC CONVERTER FOR BESS

DC-DC converter serves as an interface between the BESS and inverter DC-link. It must regulate the BESS voltage level suitable for DC-link and also carry out the control strategies for charging and discharging of the battery. Converter also needs to be bi-directional since power must flow in both directions. These requirements makes the DC-DC converter an important piece of the whole BESS scheme that should be modeled with using great care.

5.1 Choosing the topology for the bi-directional DC-DC converter

Appropriate comparative study among four basic topologies in the field of industry are introduced in [34]. Topologies compared are conventional Buck-Boost, Fly-back, Cuk and SEPIC converters from which the SEPIC was found to be most suitable choice in terms of current ripple. However, SEPIC and CUK converters require some extra components (capacitors and inductors) which increases the costs when considering commercialized product. Also complexity of the converter and the whole BESS design would be increased. Fly-back and conventional Buck-Boost are equally simple but output voltage is reversed in Fly-back converter which is not desired. Due to the foregoing aspects, conventional bi-directional Buck-Boost DC-DC converter was chosen for further analysis.

5.2 Modeling of the bi-directional buck-boost DC-DC converter in CCM

Principal circuit scheme of the bi-direction Buck-Boost DC-DC converter with input and output capacitors is presented in figure 5.1

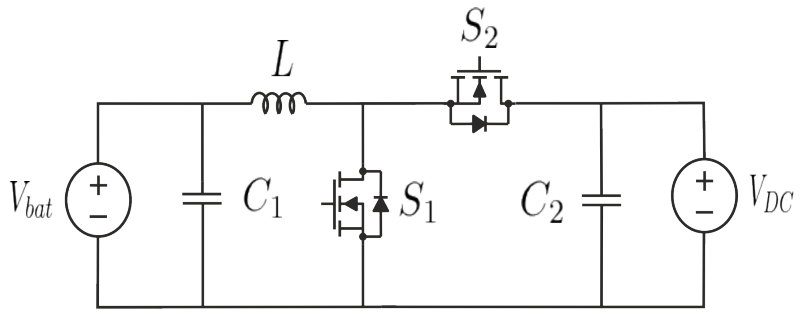

Figure 5.1 *Circuit diagram of a bi-directional Buck-Boost converter*

When working in boost mode, S_1 is operated between the conductive and non-conductive states and S_2 completely turned off. For buck mode, switches work other way around. By-pass diodes are required to allow forward-biased current to flow in the circuit when the switch is turned off. Apart from these aspects, converter is operating as individual buck or boost converter and thus these modes can be separately modeled. Modeling is done for the converter operating at CCM and operation at DCM is not considered in this thesis.

For later control design, converters input and output variables must be derived for proper design of the converter. This depends on the application, i.e. what kind of sources and loads are used and what quantity is wanted to be controlled. Different types of power sources are illustrated in figure 5.2.

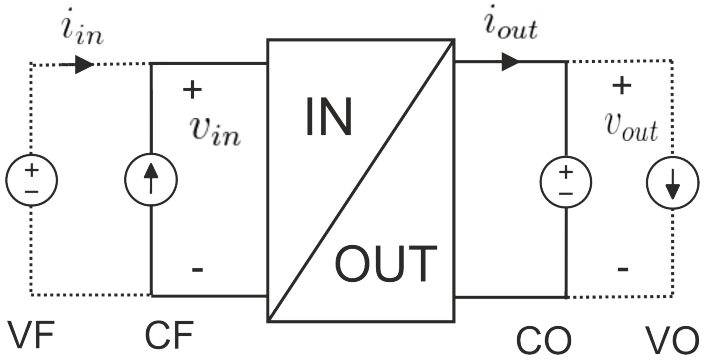

Figure 5.2 *Power source types of DC-DC converter*

Possible input source types are *voltage-fed* (VF) and *current-fed* (CF). This definition determines which one of the input side quantities is regarded as input variable of the converter other being the output variable. Output load definition on the contrary defines the output variable while other quantity is the input variable in the output side of the converter. Possible load types are *current-out* (CO) and *voltage-out* (VO) [9, 35]. Thus it can be realized that voltage and current at the input and output terminals of the converter are not the same as input and output variables of

the converter and should not be mixed together.

5.2.1 Modeling of the boost-mode

As previously mentioned, boost-mode is used during discharge of the battery. Battery is then modeled as voltage source V_{bat} feeding the inverter DC-link voltage V_{DC} which is also presumed as constant voltage source (or sink). This is not the case in reality and assumption made in terms of V_{DC} is determined by the unit that is controlling the voltage V_{DC}. However, this aspect is out of the context of this thesis and is more relevant in future research. Power source type of the boost converter can then be regarded as VF/CO since current will be the controlled output variable. During boost operation, discharge current is only limited by the battery and it's capability to supply current. Thus only VF/CO power source type is needed to model for further control design during boost mode.

Derivation of average model

Equivalent circuit model of VF/CO with included losses is illustrated in figure 5.3

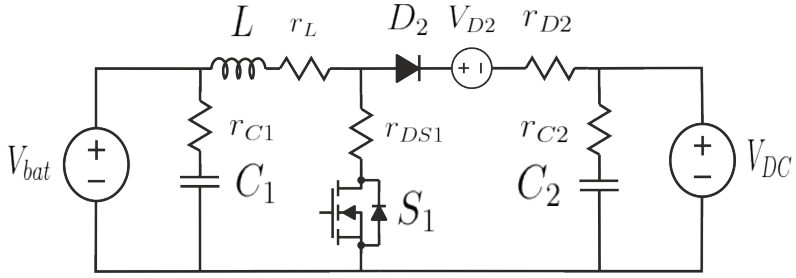

Figure 5.3 *Circuit diagram of a Boost-converter*

Boost converter circuit can be represented as two different sub-circuits due to the two different switching states of the circuit. By doing this, the switch and diode can be omitted and sub-circuits for on and off-time are shown in figure 5.4.

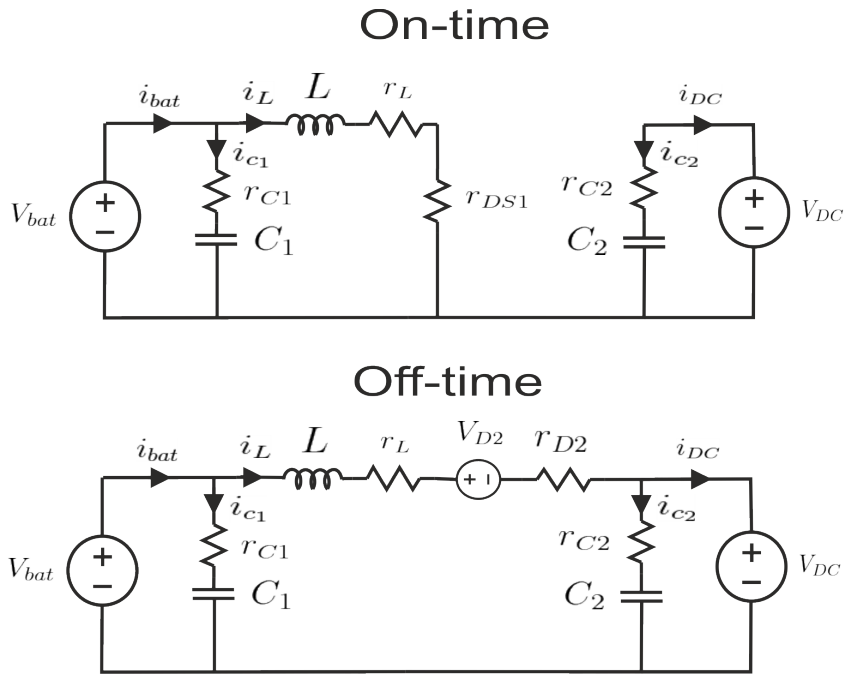

Figure 5.4 *Sub-circuits of the boost converter*

To link these two sub-circuits together, we can introduce a variable d (duty ratio) to describe the relative time that the switch is at on-state during one fundamental switching period T_s. It is also relevant to introduce duty ratio's complement d' to describe the off-state of the converter. Equations for both sub-circuits are separately derived, multiplied by their relative on-time value (either d or d') and summed together. This is the same thing as averaging and such modeling technique is called average modeling.

Now d will be regarded as input variable of the converter along with those determined by the power source type. Inductor voltages and capacitor currents are usually chosen as the state-variables of the converter. State-variables, input and output variables of the boost converter in 5.3 can be regarded as follows.

state-variables: input variables: output variables:

$$\dot{X} = \begin{bmatrix} \hat{i}_L \\ \hat{v}_{C1} \\ \hat{v}_{C2} \end{bmatrix} \qquad U = \begin{bmatrix} \hat{v}_{bat} \\ \hat{v}_{DC} \\ \hat{d} \end{bmatrix} \qquad Y = \begin{bmatrix} \hat{i}_{bat} \\ \hat{i}_{DC} \end{bmatrix} \tag{5.1}$$

By using the definitions $v_L = L\dfrac{di_L}{dt}$ and $i_c = C\dfrac{dv_C}{dt}$ for the state-variables and applying KVL and KCL for the sub-circuits in figure 5.4, we can get the following

averaged model equations for state-variable derivatives and output variables.

$$\frac{d\langle i_L\rangle}{dt} = \frac{\langle v_{bat}\rangle - (r_L - r_{DS1}d - r_D d')\langle i_L\rangle - V_D d' - \langle v_{DC}\rangle d'}{L} \tag{5.2}$$

$$\frac{d\langle v_{C1}\rangle}{dt} = \frac{\langle v_{bat}\rangle - \langle v_{C1}\rangle}{C_1 r_{C1}} \tag{5.3}$$

$$\frac{d\langle v_{C2}\rangle}{dt} = \frac{\langle v_{C2}\rangle - \langle v_{DC}\rangle}{C_2 r_{C2}} \tag{5.4}$$

$$\langle i_{bat}\rangle = \frac{\langle v_{bat}\rangle - \langle v_{C1}\rangle}{r_{C1}} + \langle i_L\rangle \tag{5.5}$$

$$\langle i_{DC}\rangle = \frac{\langle v_{C2}\rangle - \langle v_{DC}\rangle}{r_{C2}} + \langle i_L\rangle d' \tag{5.6}$$

Variables in (5.2) - (5.6) apart from d are averaged variables and denoted with brackets $\langle\rangle$.

Steady-State operation point

To be able to model the converter, these equations have to be linearized to an operating point around which the converter behaviour can be considered to be approximately linear. Sufficient point for linearization is the steady-state operation point in which the state-variable derivatives, inductor voltage and capacitor currents are zero. Thus we get the following steady-state.

$$V_{bat} = V_{C1} \tag{5.7}$$

$$V_{DC} = V_{C2} \tag{5.8}$$

$$I_{bat} = I_L \tag{5.9}$$

$$I_{DC} = I_L D' \tag{5.10}$$

Variables in (5.7) - (5.10) are denoted as uppercase letters to emphasize that they are at steady-state. For VF/CO converter, output current I_{DC} is used as a reference for the controller and it is therefore known variable. Therefore, to solve duty ratio steady-state value D from (5.2), it is more appropriate to use output current instead of inductor current. By solving I_L from (5.10) and substituting it to (5.2), following

form can be derived for inductor voltage steady-state equation.

$$V_{bat} - (r_L - r_{DS1}D - r_D D')\frac{I_{DC}}{D'} - V_D D' - V_{DC}D' = 0 \tag{5.11}$$

(5.11) can be now used to derive steady-state representation to the duty ratio. Now it is more relevant to solve the equation in terms of D'. Rearranged equation in terms of D' is shown below.

$$-(V_D + V_{DC})D'^2 + (V_{bat} - (r_D - r_{DS1})I_{DC})D' - (r_L + r_{DS1})I_{DC} = 0 \tag{5.12}$$

(5.12) is now second-order polynomial which can be solved by using a well-known quadratic formula. Second-order polynomial has usually two solutions and only one of them is appropriate for the correct operation of the converter. The right one can be concluded by picking the one that is closer to the duty ratio obtained from the ideal conversion ratio definition which is

$$V_{out} = \frac{V_{in}}{D'}. \tag{5.13}$$

Linearized averaged state-space model

Now the converter can be linearized to the steady-state operation point derived above. This can be done by taking partial derivatives of the (5.2) - (5.6) in terms of each small-signal variables while treating others as constant.

$$\frac{d\hat{i}_L}{dt} = \frac{1}{L}\hat{v}_{bat} - \frac{(r_L + r_{DS1}D + r_D D')}{L}\hat{i}_L - \frac{D'}{L}\hat{v}_{DC} + \frac{(-r_{DS1} + r_D)I_L + V_D + V_{DC}}{L}\hat{d} \tag{5.14}$$

$$\frac{d\hat{v}_{C1}}{dt} = \frac{1}{C_1 r_{C1}}\hat{v}_{bat} - \frac{1}{C_1 r_{C1}}\hat{v}_{C1} \tag{5.15}$$

$$\frac{d\hat{v}_{C2}}{dt} = \frac{1}{C_2 r_{C2}}\hat{v}_{DC} - \frac{1}{C_2 r_{C2}}\hat{v}_{C2} \tag{5.16}$$

$$\hat{i}_{bat} = \frac{1}{r_{C1}}\hat{v}_{bat} - \frac{1}{r_{C1}}\hat{v}_{C1} + \hat{i}_L \tag{5.17}$$

$$\hat{i}_{DC} = \frac{1}{r_{C2}}\hat{v}_{C2} - \frac{1}{r_{C2}}\hat{v}_{DC} + D'\hat{i}_L - I_L\hat{d} \tag{5.18}$$

Equations (5.14) - (5.18) can also be represented in matrix form as

$$\begin{bmatrix} \frac{d\hat{i}_L}{dt} \\ \frac{d\hat{v}_{C1}}{dt} \\ \frac{d\hat{v}_{C2}}{dt} \end{bmatrix} = \begin{bmatrix} \frac{-R_{eq}}{L} & 0 & 0 \\ 0 & -\frac{1}{C_1 r_{C1}} & 0 \\ 0 & 0 & -\frac{1}{C_2 r_{C2}} \end{bmatrix} \begin{bmatrix} \hat{i}_L \\ \hat{v}_{C1} \\ \hat{v}_{C2} \end{bmatrix} + \begin{bmatrix} \frac{1}{L} & -\frac{D'}{L} & \frac{V_{eq}}{L} \\ \frac{1}{C_1 r_{C1}} & 0 & 0 \\ 0 & \frac{1}{C_2 r_{C2}} & 0 \end{bmatrix} \begin{bmatrix} \hat{v}_{bat} \\ \hat{v}_{DC} \\ \hat{d} \end{bmatrix} \tag{5.19}$$

$$\begin{bmatrix} \hat{i}_{bat} \\ \hat{i}_{DC} \end{bmatrix} = \begin{bmatrix} 1 & -\frac{1}{r_{C1}} & 0 \\ D' & 0 & \frac{1}{r_{C2}} \end{bmatrix} \begin{bmatrix} \hat{i}_L \\ \hat{v}_{C1} \\ \hat{v}_{C2} \end{bmatrix} + \begin{bmatrix} \frac{1}{r_{C1}} & 0 & 0 \\ 0 & -\frac{1}{r_{C2}} & -I_L \end{bmatrix} \begin{bmatrix} \hat{v}_{bat} \\ \hat{v}_{DC} \\ \hat{d} \end{bmatrix} \tag{5.20}$$

In the matrix form, parasitic resistance term $(r_L + r_{DS1}D + r_D D')$ is denoted as R_{eq} and equivalent voltage term $(-r_{DS1} + r_D)I_L + V_D + V_{DC}$ is denoted as equivalent voltage term V_{eq}. by denoting matrixes and vectors by simply with a letter, we get the following representation.

$$\dot{\mathbf{x}}(t) = \mathbf{A}\mathbf{x}(t) + \mathbf{B}\mathbf{u}(t) \tag{5.21}$$

$$\mathbf{y}(t) = \mathbf{C}\mathbf{x}(t) + \mathbf{D}\mathbf{u}(t) \tag{5.22}$$

In (5.21) and (5.22), the matrixes are denoted as bold uppercase letters and vectors with bold lowercase letters. To develop the representation even further, equations are brought to Laplace-domain simply by replacing the derivatives with a Laplace-variable s. Also by using matrix algebra and eliminating $\mathbf{x}$, following form is obtained.

$$\mathbf{y}(s) = \left[\mathbf{C}\left[s\mathbf{I} - \mathbf{A}\right]^{-1}\mathbf{B} + \mathbf{D}\right]\mathbf{u}(s), \tag{5.23}$$

where $\mathbf{I}$ is the unit matrix with ones in it's diagonal. Moving back to matrix from will yield to

$$\begin{bmatrix} \hat{i}_{bat} \\ \hat{i}_{DC} \end{bmatrix} = \begin{bmatrix} Y_{in-o} & T_{oi-o} & G_{ci-o} \\ G_{io-o} & -Y_{o-o} & G_{co-o} \end{bmatrix} \begin{bmatrix} \hat{v}_{bat} \\ \hat{v}_{DC} \\ \hat{d} \end{bmatrix}. \tag{5.24}$$

Input-to-output description in (5.24) contains the open-loop transfer functions between input and output variables in general form [9, 35]. To better describe which inputs and outputs are at battery side and DC-link side, following form of the (5.24)

is used for this thesis.

$$\begin{bmatrix} \hat{i}_{bat} \\ \hat{i}_{DC} \end{bmatrix} = \begin{bmatrix} Y_{bat-o} & T_{DCbat-o} & G_{cbat-o} \\ G_{batDC-o} & -Y_{DC-o} & G_{cDC-o} \end{bmatrix} \begin{bmatrix} \hat{v}_{bat} \\ \hat{v}_{DC} \\ \hat{d} \end{bmatrix}. \tag{5.25}$$

Along with buck-mode dynamic transfer functions in (5.39) and (5.48), form in (5.25) is further used to design a control scheme for the converter later in section 5.3. The whole designing procedure described above is called state-space averaging originally introduced in [36].

5.2.2 Modeling of buck-mode

Unlike boost-mode, buck-mode of the converter is realized as two different power source types because of the need of constant-current constant-voltage control scheme. During constant current control, buck converter is VF/CO similar to previously modeled boost converter. During constant voltage control, converter is VF/VO. The dynamic behaviour of the converter power source types are quite different and thus they have to be separately modeled.

Buck-mode for CC-control (VF/CO)

VF/CO modeling is used for CC-control. State, input and output variables of the buck-mode are the same as was for boost-converter in (5.1) because of the same power source type (VF/CO). However, it should be noted that now battery side is the converter output and DC-link side is the input which is on the contrary to boost-mode. Equivalent circuit model of the bi-directional DC-DC converter's buck-mode working as VF/CO with included losses is illustrated in figure 5.5.

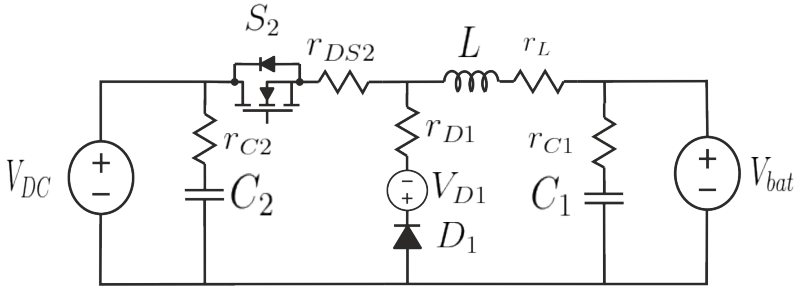

Figure 5.5 *Circuit diagram of a Buck-converter (VF/VO)*

Similar to previously modeled boost converter, also buck converter has two switching

states. These two sub-circuits are presented in figure 5.6

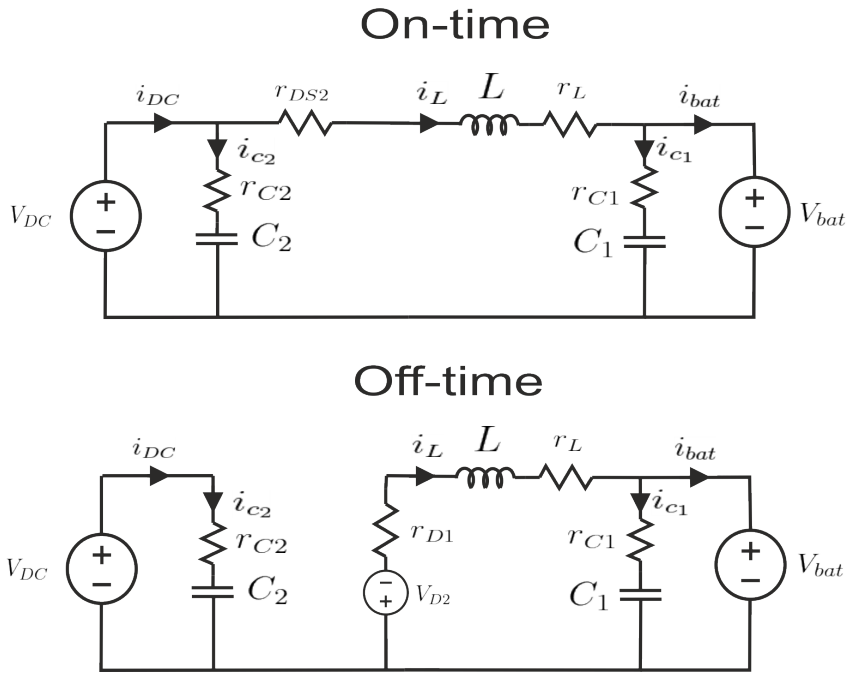

Figure 5.6 *Sub-circuits of the buck mode (VF/CO)*

Derivation of average model (VF/CO)

Averaged equations from figure 5.6 are presented below.

$$\frac{d\langle i_L\rangle}{dt} = \frac{\langle v_{DC}\rangle d - (r_L + r_{DS2}d + r_D d')\langle i_L\rangle - V_D d' - \langle v_{bat}\rangle d'}{L} \tag{5.26}$$

$$\frac{d\langle v_{C1}\rangle}{dt} = \frac{\langle v_{C1}\rangle - \langle v_{bat}\rangle}{C_1 r_{C1}} \tag{5.27}$$

$$\frac{d\langle v_{C2}\rangle}{dt} = \frac{\langle v_{DC}\rangle - \langle v_{C2}\rangle}{C_2 r_{C2}} \tag{5.28}$$

$$\langle i_{bat}\rangle = \frac{\langle v_{C1}\rangle - \langle v_{bat}\rangle}{r_{C1}} + \langle i_L\rangle \tag{5.29}$$

$$\langle i_{DC}\rangle = \frac{\langle v_{DC}\rangle - \langle v_{C2}\rangle}{r_{C2}} + \langle i_L\rangle d \tag{5.30}$$

Steady-state operation point (VF/CO)

The variables at buck-mode steady-state are obtained as follows.

$$V_{bat} = V_{C1} \tag{5.31}$$

$$V_{DC} = V_{C2} \tag{5.32}$$

$$I_{bat} = I_L \tag{5.33}$$

$$I_{DC} = I_L D' \tag{5.34}$$

$$V_{DC}D - (r_L + r_{DS2}D - r_D D')I_L - V_D D' - V_{bat} = 0 \tag{5.35}$$

To solve D inductor current must now be represented in terms of converter output current because of VF/CO power source type. Converter output is now at the battery side and relations between converter output current (I_{bat}) and inductor current unambiguous. Thus the solution for D in (5.35) is in the following first order form.

$$D = \frac{V_{bat} + V_D + (r_L + r_D)I_{bat}}{V_{DC} - (r_{DS2} - r_D)I_{bat} + V_D} \tag{5.36}$$

Linearized averaged state-space model (VF/CO)

Now the average model can be linearized to steady-state operation point and the following matrix form is obtained.

$$\begin{bmatrix} \frac{d\hat{i}_L}{dt} \\ \frac{d\hat{v}_{C1}}{dt} \\ \frac{d\hat{v}_{C2}}{dt} \end{bmatrix} = \begin{bmatrix} \frac{-R_{eq}}{L} & 0 & 0 \\ 0 & \frac{1}{C_1 r_{C1}} & 0 \\ 0 & 0 & -\frac{1}{C_2 r_{C2}} \end{bmatrix} \begin{bmatrix} \hat{i}_L \\ \hat{v}_{C1} \\ \hat{v}_{C2} \end{bmatrix} + \begin{bmatrix} \frac{1}{L} & \frac{D}{L} & \frac{V_{eq}}{L} \\ -\frac{1}{C_1 r_{C1}} & 0 & 0 \\ 0 & \frac{1}{C_2 r_{C2}} & 0 \end{bmatrix} \begin{bmatrix} \hat{v}_{bat} \\ \hat{v}_{DC} \\ \hat{d} \end{bmatrix} \tag{5.37}$$

$$\begin{bmatrix} i_{bat} \\ i_{DC} \end{bmatrix} = \begin{bmatrix} 1 & \frac{1}{r_{C1}} & 0 \\ D & 0 & -\frac{1}{r_{C2}} \end{bmatrix} \begin{bmatrix} \hat{i}_L \\ \hat{v}_{C1} \\ \hat{v}_{C2} \end{bmatrix} + \begin{bmatrix} -\frac{1}{r_{C1}} & 0 & 0 \\ 0 & \frac{1}{r_{C2}} & I_L \end{bmatrix} \begin{bmatrix} \hat{v}_{bat} \\ \hat{v}_{DC} \\ \hat{d} \end{bmatrix} \tag{5.38}$$

This can be represented in dynamic transfer-function form as was done for boost

converter in equation (5.23).

$$\begin{bmatrix} i_{bat} \\ i_{DC} \end{bmatrix} = \begin{bmatrix} -Y_{bat-o} & G_{DCbat-o} & G_{cDC-o} \\ T_{batDC-o} & Y_{DC-o} & G_{cbat-o} \end{bmatrix} \begin{bmatrix} \hat{v}_{bat} \\ \hat{v}_{DC} \\ \hat{d} \end{bmatrix} \tag{5.39}$$

Buck-mode for CV-control (VF/VO)

Problematic issue with CV-control mode is that battery voltage should be controlled which means that it is chosen as output variable for the modeling. However, battery characteristics are similar to constant voltage sink/source as was the case with previous current control modes. This would result battery voltage to appear as variable in the input side also. This would lead to a trivial solution $\hat{v}_{out} = \hat{v}_{in}$. This situation would not actually represent any of the power source type presented in figure 5.2 but a parasitic loss component in the battery side would introduce a voltage drop between input and output of such system that would solve the problem. Battery internal impedance appearing as load effect can be yielded as such parasitic component. VF/VO however has similar dynamic characteristics and is therefore used here. Change of variable can be later applied to the derived model when load-effect is taken into account in section 5.4.3 and the relation between $\hat{v}_{out}$ and $\hat{v}_{in}$ is not trivial in a sense.

State, input and output variables of VF/VO buck converter are presented below.

state-variables: input variables: output variables:

$$\dot{X} = \begin{bmatrix} \hat{i}_L \\ \hat{v}_{C1} \\ \hat{v}_{C2} \end{bmatrix} \qquad U = \begin{bmatrix} \hat{i}_{bat} \\ \hat{v}_{DC} \\ \hat{d} \end{bmatrix} \qquad Y = \begin{bmatrix} \hat{v}_{bat} \\ \hat{i}_{DC} \end{bmatrix} \tag{5.40}$$

Now battery voltage is the output variable. This means that $\hat{v}_{bat}$ cannot be used in the averaged model and it must be defined in terms of i_{bat}. Equivalent circuit model of the bi-directional DC-DC converter's buck-mode working as VF/VO with included losses and it's two sub-circuits are illustrated in figure 5.7 and 5.8.

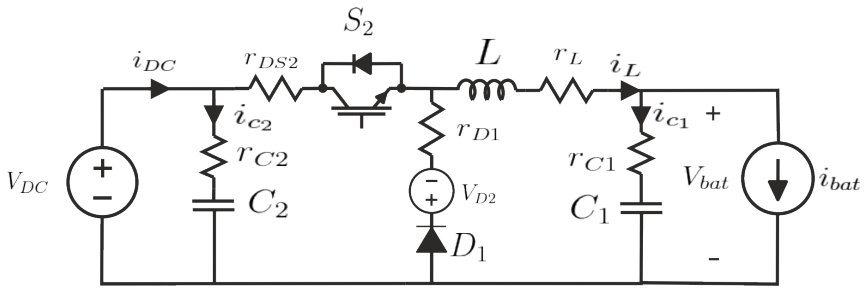

Figure 5.7 *Circuit diagram of a Buck-converter (VF/VO)*

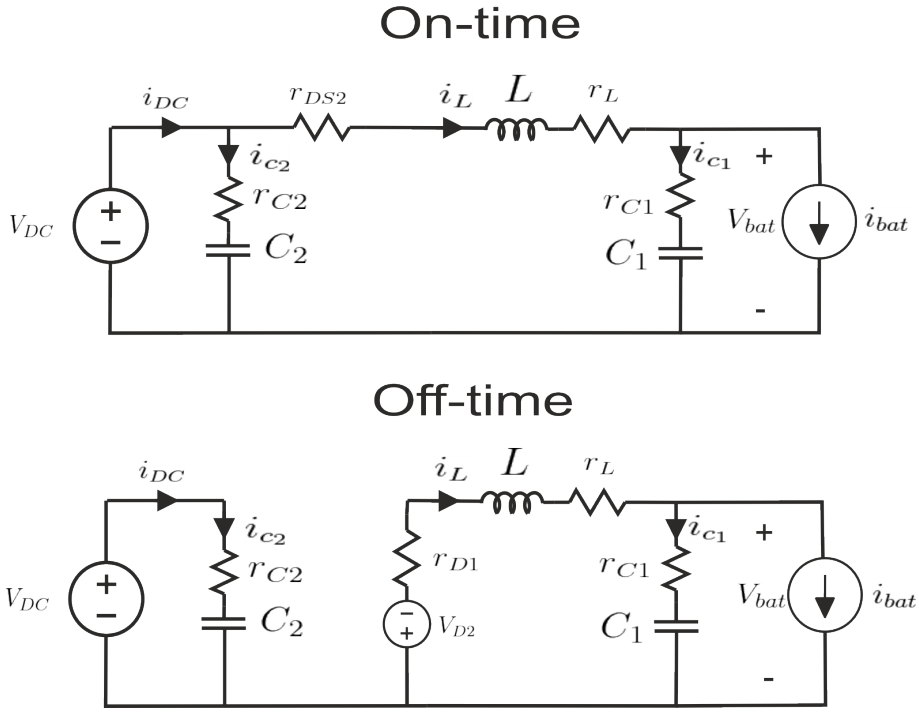

Figure 5.8 *Sub-circuits of the buck mode (VF/VO)*

Derivation of average model (VF/VO)

Average model equations of the VF-VO buck-converter are shown below.

$$\frac{d\langle i_L\rangle}{dt} = \frac{\langle v_{DC}\rangle d - (r_L + r_{DS1}d + r_D d')\langle i_L\rangle - V_D d' - \langle v_{C1}\rangle - r_{C1}(\langle i_L\rangle - \langle i_{bat}\rangle)}{L} \tag{5.41}$$

$$\frac{d\langle v_{C1}\rangle}{dt} = \frac{\langle i_L\rangle - \langle i_{bat}\rangle}{C_1} \tag{5.42}$$

$$\frac{d\langle v_{C2}\rangle}{dt} = \frac{\langle v_{DC}\rangle - \langle v_{C2}\rangle}{C_2} \tag{5.43}$$

$$\langle v_{bat}\rangle = \langle v_{C1}\rangle + r_{C1}(\langle i_L\rangle - \langle i_{bat}\rangle) \tag{5.44}$$

$$\langle i_{DC}\rangle = \frac{\langle v_{DC}\rangle - \langle v_{C2}\rangle}{r_{C2}} + \langle i_L\rangle d \tag{5.45}$$

Steady-State Operation Point and Linearized Averaged State-Space Model (VF/VO)

Steady-state values obtained from above equations are exactly the same as was for VF/CO buck-converter in (5.31) - (5.35). Thus these can be used further and linearized state-space equations can be derived and are represented below in matrix form.

$$\begin{bmatrix} \frac{d\hat{i}_L}{dt} \\ \frac{d\hat{v}_{C1}}{dt} \\ \frac{d\hat{v}_{C2}}{dt} \end{bmatrix} = \begin{bmatrix} \frac{-R_{eq}}{L} & -\frac{1}{L} & 0 \\ \frac{1}{C1} & 0 & 0 \\ 0 & 0 & -\frac{1}{C_2 r_{C2}} \end{bmatrix} \begin{bmatrix} \hat{i}_L \\ \hat{v}_{C1} \\ \hat{v}_{C2} \end{bmatrix} + \begin{bmatrix} \frac{r_{C1}}{L} & \frac{D}{L} & \frac{V_{eq}}{L} \\ -\frac{1}{C_1} & 0 & 0 \\ 0 & \frac{1}{C_2 r_{C2}} & 0 \end{bmatrix} \begin{bmatrix} \hat{i}_{bat} \\ \hat{v}_{DC} \\ \hat{d} \end{bmatrix} \tag{5.46}$$

$$\begin{bmatrix} \hat{v}_{bat} \\ \hat{i}_{DC} \end{bmatrix} = \begin{bmatrix} r_{C1} & 1 & 0 \\ D & 0 & -\frac{1}{r_{C2}} \end{bmatrix} \begin{bmatrix} \hat{i}_L \\ \hat{v}_{C1} \\ \hat{v}_{C2} \end{bmatrix} + \begin{bmatrix} -r_{C1} & 0 & 0 \\ 0 & \frac{1}{r_{C2}} & I_L \end{bmatrix} \begin{bmatrix} \hat{i}_{bat} \\ \hat{v}_{DC} \\ \hat{d} \end{bmatrix} \tag{5.47}$$

The equivalent resistance term R_{eq} is now denoted as $(r_L + r_{C1} + r_{DS1}d + r_D d')$. Finally we get the dynamic transfer function form by using the equation (5.23).

$$\begin{bmatrix} \hat{v}_{bat} \\ \hat{i}_{DC} \end{bmatrix} = \begin{bmatrix} -Z_{bat-o} & G_{DCbat-o} & G_{cbat-o} \\ T_{batDC-o} & Y_{DC-o} & G_{cDC-o} \end{bmatrix} \begin{bmatrix} \hat{i}_{bat} \\ \hat{v}_{DC} \\ \hat{d} \end{bmatrix} \tag{5.48}$$

5.3 Control scheme for the bi-directional DC-DC converter

In this section, proper control design is implemented for the bi-directional DC-DC converter. Altogether, there are three different modes of operation in which the control scheme should be derived separately. These are the discharge mode, constant current charging mode and constant voltage charging mode also known as constant-current-costant-voltage (CC-CV) charging mode [18, 37].

5.3.1 Loop-shaping technique for control design

In this thesis, control loops for all operation modes are tuned using *loop-shaping* control design technique useful for PI-controllers. In loop-shaping technique, control-loop margins are shaped by inserting additional poles and zeros with a gain in the controller transfer function. Results are then observed visually from bode plot of the control loop. PI-controller can be represented in terms of gain term, zeros and poles as follows.

$$G_{cc}(s) = K_{cc}\frac{(\frac{s}{\omega_{z1}}+1)(\frac{s}{\omega_{z2}}+1)}{s(\frac{s}{\omega_{p1}}+1)(\frac{s}{\omega_{p2}}+1)} \tag{5.49}$$

In (5.49), K is the gain of the controller. ω_{z1} and ω_{z2} are the frequencies of the zeros and ω_{p1} and ω_{p2} are the poles of the controller transfer function as angular frequency $2\pi f$. Single s in the denominator represents the integrator of the PI-controller and it also can be interpret as pole placed at origo. Controller in (5.49) must always have lower or equal number of zeros than poles to make the controller realizable. In terms of this thesis, a reduced-order controller is used with one zero and pole, integrator and gain as

$$G_{cc}(s) = K_{cc}\frac{(\frac{s}{\omega_{z1}}+1)}{s(\frac{s}{\omega_{p1}}+1)}, \tag{5.50}$$

with which an acceptable performance can be achieved for the converter. To realize controller in (5.50) as PI-controller and low-pass filter (effect of poles), following

relation can be used .

$$K_{cc}\frac{(\frac{s}{\omega_z}+1)}{s(\frac{s}{\omega_p}+1)} \Longleftrightarrow (\frac{K_{cc}}{\omega_z}+\frac{K_{cc}}{s})\frac{1}{\frac{s}{\omega_p}+1} \Longleftrightarrow (K_p+\frac{K_I}{s})(\frac{1}{\frac{s}{\omega_p}+1}) \tag{5.51}$$

$$\Longrightarrow \quad K_p = \frac{K_{cc}}{\omega_z} \tag{5.52}$$

$$\Longrightarrow \quad K_I = K_{cc} \tag{5.53}$$

In (5.51), first term in the brackets is the conventional PI-controller with proportional gain K_P and integral gain K_I. Second term is a first-order low-pass filter with bandwidth of ω_p.

Both zeros and poles have different effect on the control loop. Also their location in the complex plane especially in terms of imaginary axis has significant effect. Zeros and poles can be whether in the *left half plane* (LHP) or at the *right half plane* (RHP). Bode plots of the LHP- and RHP-zeros and -poles at frequency $\omega = 2\pi 1000Hz$ are illustrated in figures 5.9 and 5.10.

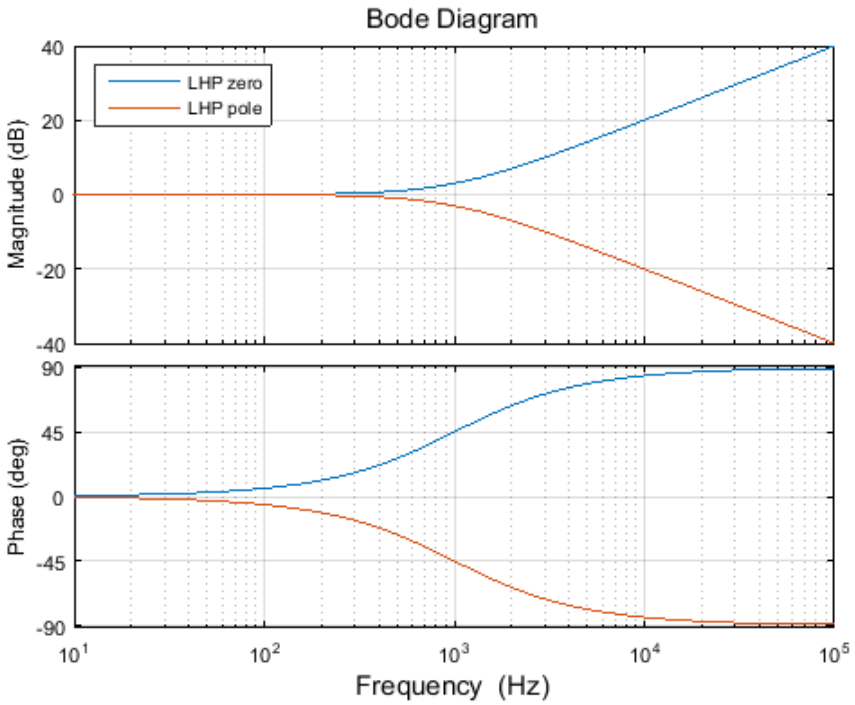

Figure 5.9 *Bode plots of the LHP-zeros and -poles*

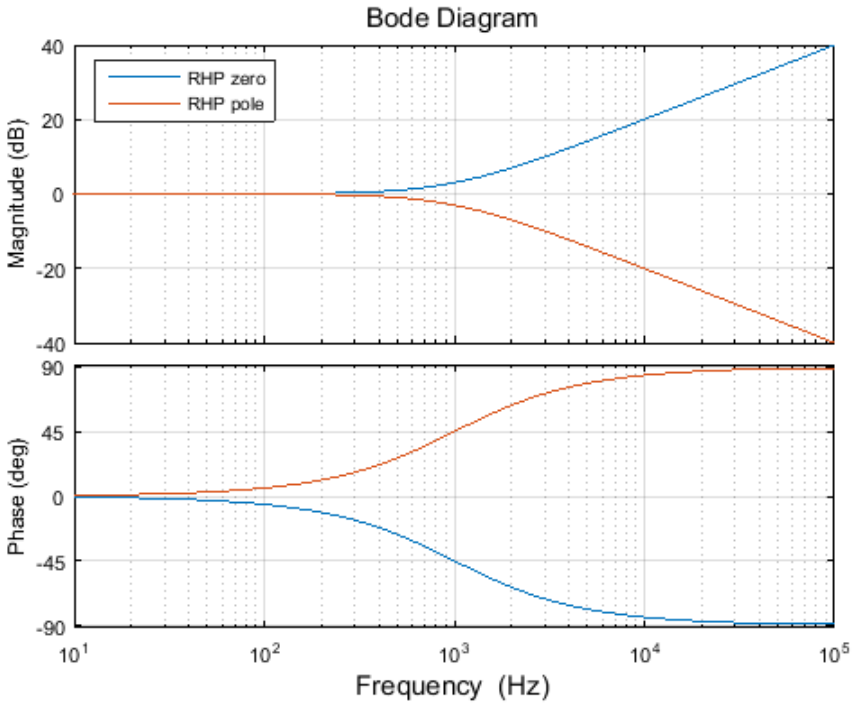

Figure 5.10 *Bode plots of the RHP-zeros and -poles*

It can be concluded from figure 5.9 that LHP-zeros give both gain and phase boost for the controller. Gain boost is 20dB/decade starting at the zero frequency ω_z and phase boost is up to 90° starting one decade before and being 45° at ω_z. LHP-poles' frequency response is behaving in the opposite manner than for zeros' which is realized as filtering features. For RHP-zeros and -poles, phase behaviour is reversed to LHP-zeros and poles. RHP-zeros and -poles may be involved in converter dynamics by default but these are never intentionally added to controllers because they tend to drive the converter towards instability [9].

Control loops are usually tuned in terms of cross-over frequency, gain margin (GM) and phase margin (PM). Cross-over frequency of the control loop is the frequency at which the gain plot has 0dB magnitude. Phase margin is the phase gap between the phase at cross-over frequency and the $-180°$-point. Gain margin is simply the gain at the $-180°$-point. It yields that gain margin should be negative and phase margin positive to ensure stability of the control loop and the whole converter.

Cross-over frequency of the control loop determines the speed of the converter which often should be as high as possible. On the other hand, too fast control loop allows disturbances to get pass the controller and cause instability. Phase margin has also effect on the controller speed but moreover to the amount of overshoot in a

step response. higher phase margin will yield to smaller overshoot but also to slower response. Phase margin is often chosen to equal 65° which is a good trade-off between the amount of overshoot and speed it's deeper meaning lying on the characteristics of second-order polynomial [9]. This 65° PM is not reached in the control design here because the aim is to use same controller for all control modes as is realized further.

5.3.2 Current control for discharge of the battery (without source- and load effect)

For discharge of the battery, output current control is used to provide desired current to the DC-link. Now $\hat{i}_{DC}$ is the output current. Let us consider the definition of $\hat{i}_{DC}$ for boost-mode in (5.25).

$$\hat{i}_{DC} = G_{batDC-o}\hat{v}_{bat} - Y_{DC-o}\hat{v}_{DC} + G_{cDC-o}\hat{d} \tag{5.54}$$

In terms of control design, the output variable $\hat{i}_{DC}$ can be manipulated by manipulating the control-to-output transfer function G_{cDC-o}. This is realized as follows

$$G_{CO} = G_{cDC-o}G_{cc} \tag{5.55}$$

G_{CO} is now the control loop which needs to be tuned by applying loop-shaping technique. When using converter values given in table 6.3 and using the modeling technique introduced in section 5.2, following bode plot is obtained for G_{cDC-o}.

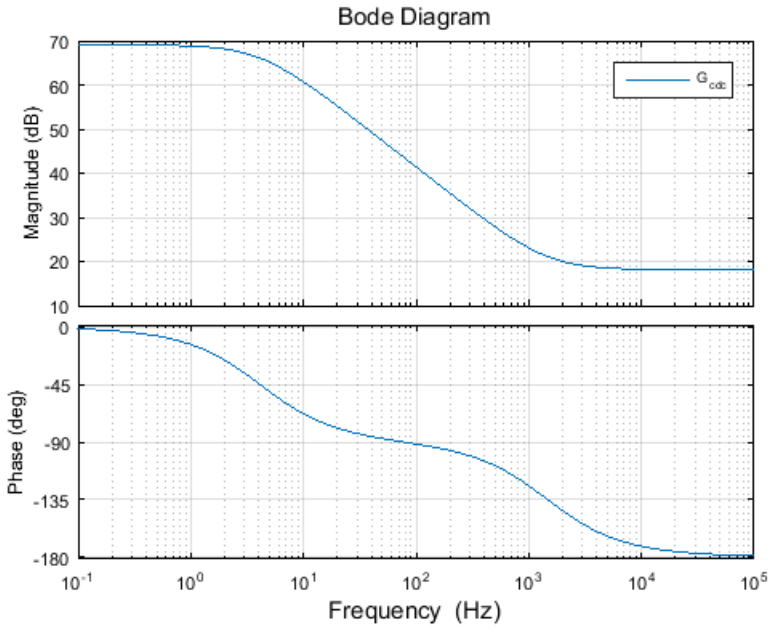

Figure 5.11 *Bode plot of the boost-mode output current control-to-output transfer function (VF/CO)*

It can be seen that G_{cDC-o} has positive magnitude within the whole frequency range which have to be limited since phase is dropping down to $-180°$. Cross-over should be lower than the beginning of the flat region at higher frequency. It also must be kept in mind that the controller will introduce 90° phase lag to the control loop if controller is introduced with one order higher denominator than numerator. 65° PM can thus be set by inserting zero to a frequency where phase $\phi = -180° + 65° + 45° = -70°$. This would however yield to relatively low cross over frequency. A good trade off for the zero frequency is selected to equal $\omega_{z1} = 2\pi 100Hz$ which will reduce PM but cross-over frequency can be increased to make the control faster. A pole is also inserted in order to filter out switching noise. A good guideline for pole frequency is $\frac{1}{8} f_{sw}$ which would correspond to $\omega_{p1} = 2\pi * 1875Hz$ [9]. Gain will be then selected to adjust the cross-over frequency to the local maximum formed to the phase response which is gives 51.8° PM. Fore-mentioned is obtained by inserting $K_{cc} = 12.45$ which will correspond to cross-over frequency $f_{cross} = 252Hz$. Corresponding control loop is shown in figure 5.12.

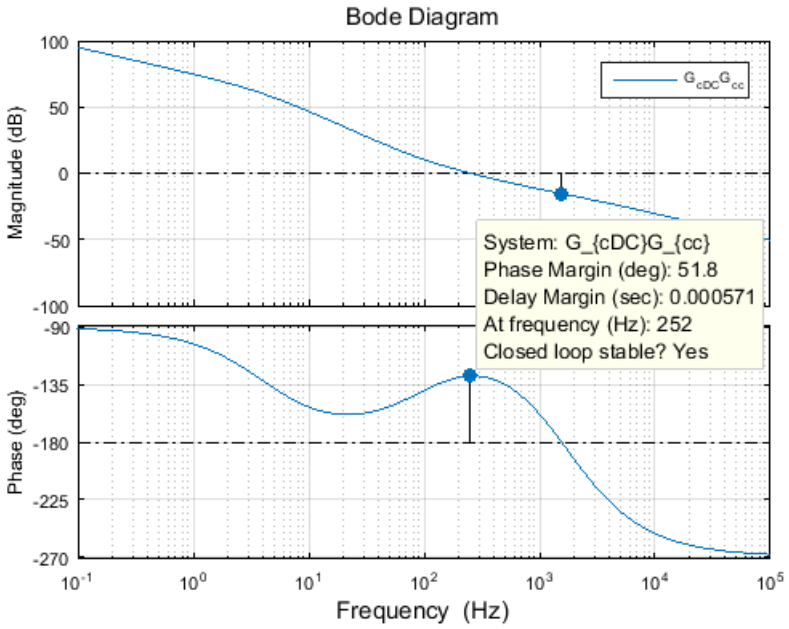

Figure 5.12 *Bode plot of the tuned control loop for boost-mode output current control (VF/CO)*

5.3.3 CC-control for charge of the battery (without source- and load effect)

For charge mode, direction of the power flow is changed and battery side is the converter output in DC-link side is the input. For CC-mode, control loop is realized by the G_{cbat-o} from the equation (5.39) and is illustrated in figure 5.13.

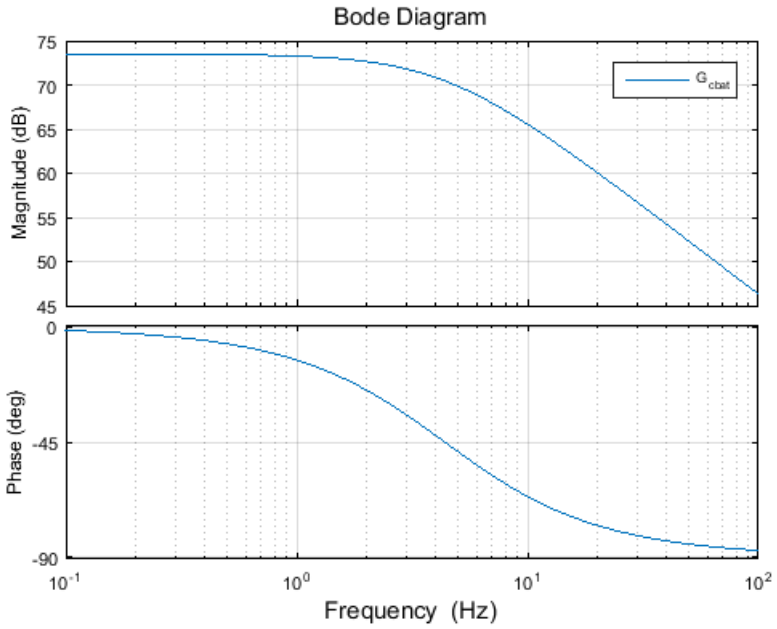

Figure 5.13 *Bode plot of the buck-mode output current control-to-output transfer function*

Bode plot in 5.13 has very similar shape to that in boost converter. However, G_{cbat} is stable as it is since phase differs between $0°$ and $-90°$ and even the integrator in the controller will not make it go beyond $-180°$-point. Same controller parameters can thus be used for CC-control during charge as for CC-control during battery discharge. By using the same controllers, following bode plot is obtained.

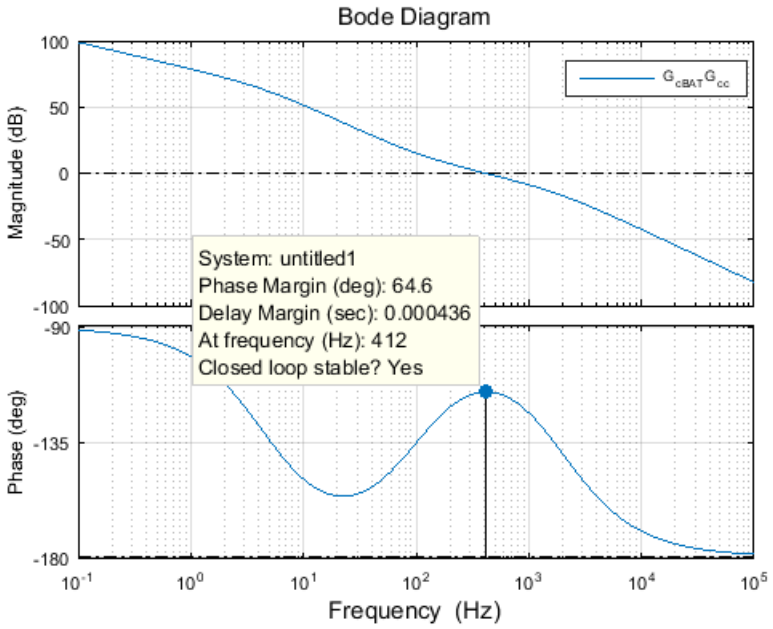

Figure 5.14 *Bode plot of the tuned control loop for buck-mode output current control (VF/CO)*

It can be seen that same controller parameters will yield to higher PM (65°) and higher cross-over frequency ($412Hz$).

5.3.4 CV-control for charge of the battery (without source- and load effect)

As was already stated in section 5.2.2, CV-control cannot be realized with battery modeled as non-linear voltage source/sink in the ideal case but have to be modeled with i.e. load effect to introduce a voltage difference between converter input and output variable. Thus CV-control is eventually derived with load effect in section 5.4.3

5.4 Load and Source-Effect of Battery to DC-DC Converter

DC-DC converters are always used as a link between input source and output load power flowing from source to load through the converter. These sources and loads are often modelled as constant power sources or sinks which they never are. There may be parasitic internal output or input impedances or some other devices, cascaded that will affect to these input and output characteristics of DC-DC converter [10,35].

Battery with parasitic internal impedance can be well regarded as good example of such system. Principal scheme of a converter with different source and load types is illustrated in figure 5.15.

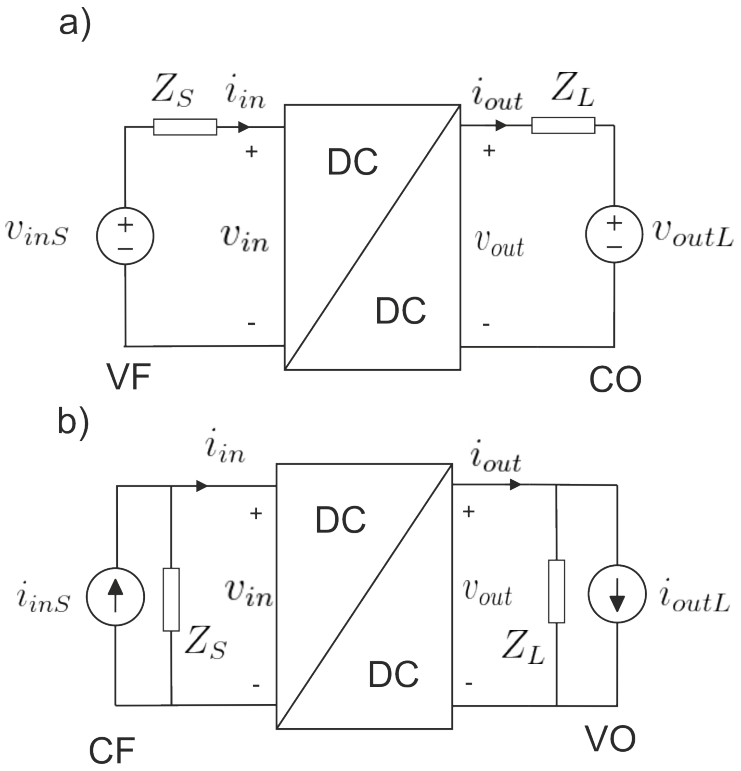

Figure 5.15 *Principal scheme of DC-DC converter including parasitic elements at source and load with* ***a)*** *voltage-fed source and load* ***b)*** *current-fed source and load*

In figure 5.15, uppercase notations in the quantities yields to quantity at source side (S) or load side (L).

5.4.1 Source effect of the battery impedance in boost mode

By applying KVL to circuit in figure 5.15 we get

$$\hat{v}_{batS} - Z_S\hat{i}_{bat} - \hat{v}_{bat} = 0 \quad \Longleftrightarrow \quad \hat{v}_{bat} = \hat{v}_{batS} - Z_S\hat{i}_{bat}. \tag{5.56}$$

This definition of $\hat{v}_{bat}$ can be further substituted to equation (5.25) where the output variables can be now represented as follows.

$$\hat{i}_{bat} = Y_{bat-o}(\hat{v}_{batS} - Z_S\hat{i}_{bat}) + T_{DCbat-o}\hat{v}_{DC} + G_{cbat-o}\hat{d} \tag{5.57}$$

$$\hat{i}_{DC} = G_{batDC-o}(\hat{v}_{batS} - Z_S\hat{i}_{bat}) - Y_{DC-o}\hat{v}_{DC} + G_{cDC-o}\hat{d} \tag{5.58}$$

New input variable $\hat{v}_{batS}$ is now introduced to both output variable equations instead of $\hat{v}_{bat}$. By rearranging the terms first in (5.57), we get

$$\hat{i}_{bat} = \frac{Y_{bat-o}}{1 + Z_S Y_{bat-o}} \hat{v}_{batS} + \frac{T_{DCbat-o}}{1 + Z_S Y_{bat-o}} \hat{v}_{DC} + \frac{G_{cbat-o}}{1 + Z_S Y_{bat-o}} \hat{d}, \tag{5.59}$$

which is now the source-affected expression for battery current $\hat{i}_{bat}$. $\hat{i}_{bat}$ is now also used to define DC-link current in (5.58) which must be eliminated by substituting (5.59) to (5.58) in order to get similar representation for $\hat{i}_{DC}$. By doing so and rearranging the terms, we get

$$\begin{aligned} \hat{i}_{DC} = \frac{G_{batDC-o}}{1 + Z_S Y_{bat-o}} \hat{v}_{batS} - (Y_{DC-o} - \frac{G_{batDC-o} Z_S T_{DCbat}}{1 + Z_S Y_{bat-o}}) \hat{v}_{DC} \\ + (G_{cDC-o} - \frac{G_{batDC-o} Z_S G_{cbat}}{1 + Z_S Y_{bat-o}}) \hat{d} \end{aligned} \tag{5.60}$$

Equations (5.59) and (5.60) can be also expressed in matrix form.

$$\begin{bmatrix} \hat{i}_{bat} \\ \hat{i}_{DC} \end{bmatrix} = \begin{bmatrix} \frac{Y_{bat-o}}{1 + Z_S Y_{bat-o}} & \frac{T_{DCbat-o}}{1 + Z_S Y_{bat-o}} & \frac{G_{cbat-o}}{1 + Z_S Y_{bat-o}} \\ \frac{G_{batDC-o}}{1 + Z_S Y_{bat-o}} & -Y_{DC-o} + \frac{G_{batDC-o} Z_S T_{DCbat}}{1 + Z_S Y_{bat-o}} & G_{cDC-o} - \frac{G_{batDC-o} Z_S G_{cbat}}{1 + Z_S Y_{bat-o}} \end{bmatrix} \begin{bmatrix} \hat{v}_{batS} \\ \hat{v}_{DC} \\ \hat{d} \end{bmatrix} \tag{5.61}$$

Now each source-affected transfer function contains a term $1 + Z_S Y_{bat-o}$ in the denominator. When now substituting $Z_S = 0$ all transfer functions will reduce to an original form in equation (5.25). As a comparison boost mode control loops are plotted without and with source-effect at two different SOC's (20% and 75%) in figure 5.16.

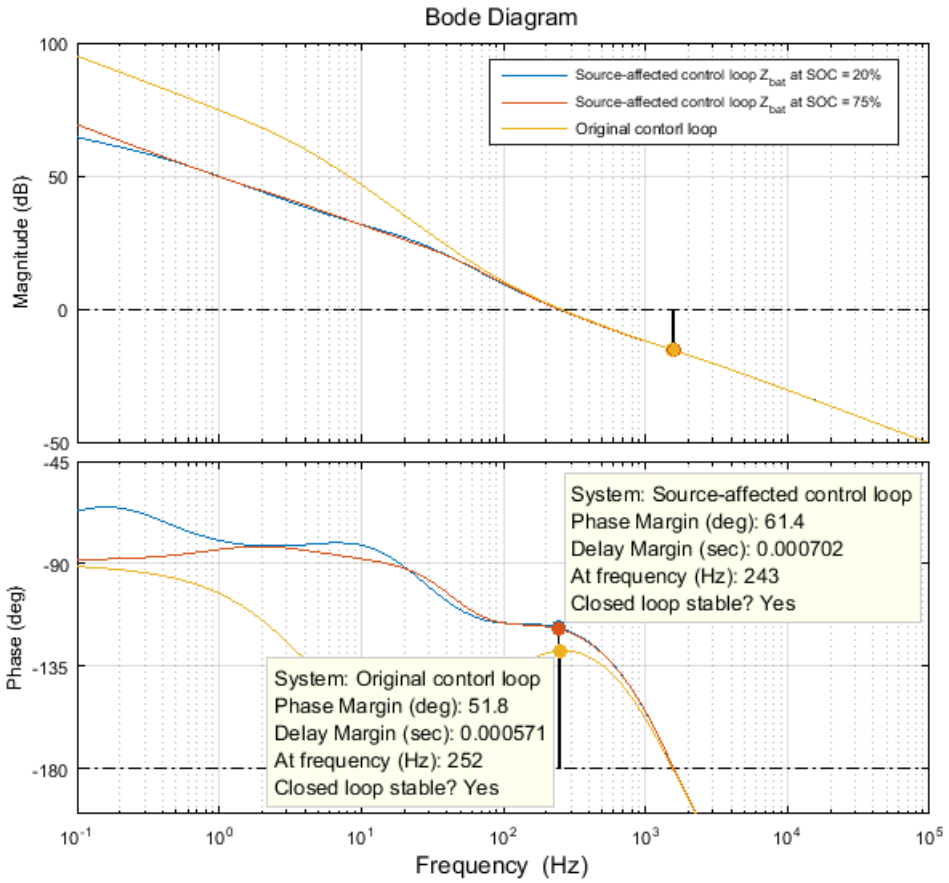

Figure 5.16 *Source-affected control loops at different SOC and original unaffected control loops during boost CC-mode*

It can be seen that source-effect damps the converter and increases the phase margin by 10° while cross-over is remained the same. In theory this would reduce the amount of overshoot in the time-domain response without slowing down the controller which can be considered as a benefit. There is no significant effect between the control loops with battery impedance as source effect.

5.4.2 Load effect of the battery impedance in buck-mode (CC)

By applying KVL to circuit in figure 5.15 we get

$$-\hat{v}_{bat} + \hat{v}_{batL} + Z_L\hat{i}_{bat} = 0 \quad \Longleftrightarrow \quad \hat{v}_{bat} = \hat{v}_{batL} + Z_L\hat{i}_{bat}. \tag{5.62}$$

This definition of $\hat{v}_{bat}$ can be further substituted to equation (5.39) where the output

variables can be now represented as follows.

$$\hat{i}_{bat} = -Y_{bat-o}(\hat{v}_{batL} + Z_L\hat{i}_{bat}) + T_{DCbat-o}\hat{v}_{DC} + G_{cbat-o}\hat{d} \tag{5.63}$$

$$\hat{i}_{DC} = G_{batDC-o}(\hat{v}_{batL} + Z_L\hat{i}_{bat}) + Y_{DC-o}\hat{v}_{DC} + G_{cDC-o}\hat{d} \tag{5.64}$$

New input variable $\hat{v}_{batL}$ is now introduced to both output variable equations instead of $\hat{v}_{bat}$. By rearranging the terms first in (5.63), we get

$$\hat{i}_{bat} = -\frac{Y_{bat-o}}{1 + Z_L Y_{bat-o}}\hat{v}_{batS} + \frac{T_{DCbat-o}}{1 + Z_L Y_{bat-o}}\hat{v}_{DC} + \frac{G_{cbat-o}}{1 + Z_L Y_{bat-o}}\hat{d}, \tag{5.65}$$

which is now the load-affected expression for battery current $\hat{i}_{bat}$. This expression would be enough to investigate the load effect to the battery current control but for clarification the whole load-affected set of transfer function are derived also for i_{DC}. Similar to before validated source effect, $\hat{i}_{bat}$ is now also used to define DC-link current in (5.64) which must be eliminated by substituting (5.65) to (5.64). By doing so and rearranging the terms, we get

$$\hat{i}_{DC} = (T_{batDC-o} - \frac{T_{batDC-o}Z_L Y_{bat-o}}{1 + Z_L Y_{bat-o}})\hat{v}_{batS} + (Y_{DC-o} - \frac{T_{batDC-o}Z_L G_{DCbat}}{1 + Z_L Y_{bat-o}})\hat{v}_{DC}$$

$$+(G_{cDC-o} - \frac{T_{batDC-o}Z_L G_{cbat}}{1 + Z_L Y_{bat-o}})\hat{d} \tag{5.66}$$

Thus we get the following load-affected set of transfer functions.

$$\begin{bmatrix} \hat{i}_{bat} \\ \hat{i}_{DC} \end{bmatrix} = \begin{bmatrix} \frac{Y_{bat-o}}{1 + Z_L Y_{bat-o}} & \frac{T_{DCbat-o}}{1 + Z_L Y_{bat-o}} & \frac{G_{cbat-o}}{1 + Z_L Y_{bat-o}} \\ \frac{G_{batDC-o}}{1 + Z_L Y_{bat-o}} & -Y_{DC-o} + \frac{G_{batDC-o}Z_L T_{DCbat}}{1 + Z_L Y_{bat-o}} & G_{cDC-o} - \frac{G_{batDC-o}Z_L G_{cbat}}{1 + Z_L Y_{bat-o}} \end{bmatrix} \begin{bmatrix} \hat{v}_{batS} \\ \hat{v}_{DC} \\ \hat{d} \end{bmatrix} \tag{5.67}$$

Now each source-affected transfer function contains a term $1 + Z_L Y_{bat-o}$ in the de-

nominator similar to boost mode. Also these new load-affected transfer functions will reduce to original unaffected form when substituting $Z_L = 0$. As a comparison, buck CC-mode control loops are plotted without and with source-effect at two different SOC's (20% and 75%) in figure 5.17.

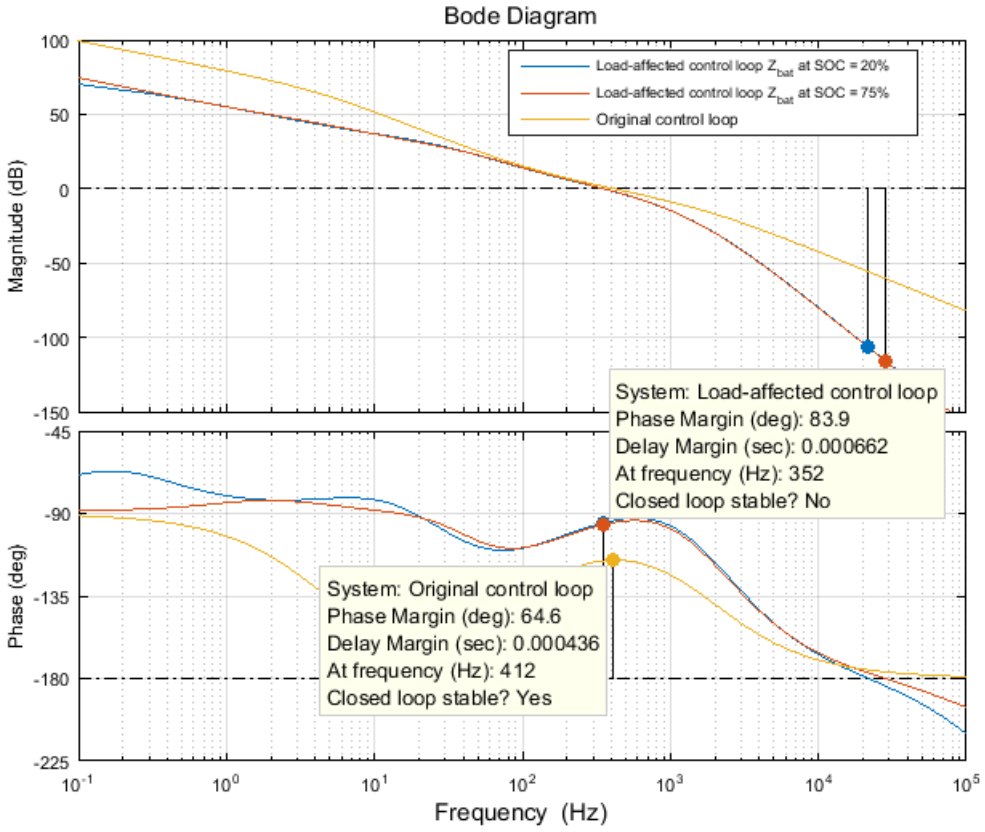

Figure 5.17 *Load-affected control loops at different SOC and original unaffected control loops during buck CC-mode*

Similar to boost mode source-effect, the load-effect here also damps the converter by increasing PM by 20° but now also cross-over frequency is shifted to lower frequencies which.

5.4.3 Load effect of the battery impedance in buck-mode (CV)

Because of the battery voltage being the output of the converter during CV-control, equation (5.62) must be solved in terms of $\hat{i}_{bat}$ which yields to

$$\hat{i}_{bat} = \frac{\hat{v}_{bat} - \hat{v}_{batL}}{Z_L} \tag{5.68}$$

By further substituting this definition to $\hat{v}_{bat}$ equation (5.48), we get

$$\hat{v}_{bat} = -Z_{bat-o}\frac{\hat{v}_{bat} - \hat{v}_{batL}}{Z_L} + T_{DCbat-o}\hat{v}_{DC} + G_{cbat-o}\hat{d} \tag{5.69}$$

$$\hat{i}_{DC} = G_{batDC-o}\frac{\hat{v}_{bat} - \hat{v}_{batL}}{Z_L} + Y_{DC-o}\hat{v}_{DC} + G_{cDC-o}\hat{d}. \tag{5.70}$$

By rearranging the terms first in (5.69) yields to

$$\hat{v}_{bat} = -\frac{Z_{bat-o}}{Z_{bat-o} + Z_L}\hat{v}_{batL} + \frac{G_{DCbat-o}Z_L}{Z_{bat-o} + Z_L}\hat{v}_{DC} + \frac{G_{cbat-o}Z_L}{Z_{bat-o} + Z_L}\hat{d}, \tag{5.71}$$

which is now the load-affected expression for battery voltage $\hat{v}_{bat}$. To get load-affected expression also for i_{DC}, load-affected battery voltage in (5.71) must be substituted to equation (5.70). By doing so and rearranging the terms, we get

$$\begin{aligned}\hat{i}_{DC} = (-\frac{T_{batDC-o}}{Z_L} + \frac{T_{batDC-o}Z_{bat-o}}{Z_L(Z_L + Z_{bat-o})})\hat{v}_{batS} \\ +(Y_{DC-o} + \frac{T_{batDC-o}G_{DCbat}}{Z_L + Z_{bat-o}})\hat{v}_{DC} + (G_{cDC-o} + \frac{T_{batDC-o}G_{cbat}}{Z_L + Z_{bat-o}})\hat{d}\end{aligned} \tag{5.72}$$

Thus we get the following load-affected set of transfer functions

$$\begin{bmatrix}\hat{v}_{bat} \\ \hat{i}_{DC}\end{bmatrix} = \begin{bmatrix}Z_{bat-load-o} & G_{DCbat-load-o} & G_{cbat-load-o} \\ T_{batDC-load-o} & Y_{DC-load-o} & G_{cDC-load-o}\end{bmatrix}\begin{bmatrix}\hat{v}_{batS} \\ \hat{v}_{DC} \\ \hat{d}\end{bmatrix}, \tag{5.73}$$

where new load-affected transfer functions are defined as follows.

$$Z_{bat-load-o} = -\frac{Z_{bat-o}}{Z_{bat-o} + Z_L} \tag{5.74}$$

$$G_{DCbat-load-o} = \frac{G_{DCbat-o} Z_L}{Z_{bat-o} + Z_L} \tag{5.75}$$

$$G_{cbat-load-o} = \frac{G_{cbat-o} Z_L}{Z_{bat-o} + Z_L} \tag{5.76}$$

$$T_{batDC-load-o} = -\frac{T_{batDC-o}}{Z_L} + \frac{T_{batDC-o} Z_{bat-o}}{Z_L (Z_L + Z_{bat-o})} \tag{5.77}$$

$$Y_{DC-load-o} = Y_{DC-o} + \frac{T_{batDC-o} G_{DCbat}}{Z_L + Z_{bat-o}} \tag{5.78}$$

$$G_{cDC-load-o} = G_{cDC-o} + \frac{T_{batDC-o} G_{cbat}}{Z_L + Z_{bat-o}} \tag{5.79}$$

$$\tag{5.80}$$

Unlike with source effect on boost-mode and load effect on CC-mode, these transfer functions do not reduce to original open-loop transfer functions when setting Z_L to zero. This is due to the triviality of the controlled output variable and input variable of the converter. To illustrate the situation, load-affected transfer function $G_{cbat-load-o}$ is shown in figure 5.18 with measured battery impedance at SOC = 75% and with $Z_L = 1e^{-13}\Omega \approx 0\Omega$. Also the original G_{cbat} from the equation (5.48) is visualized in the same figure.

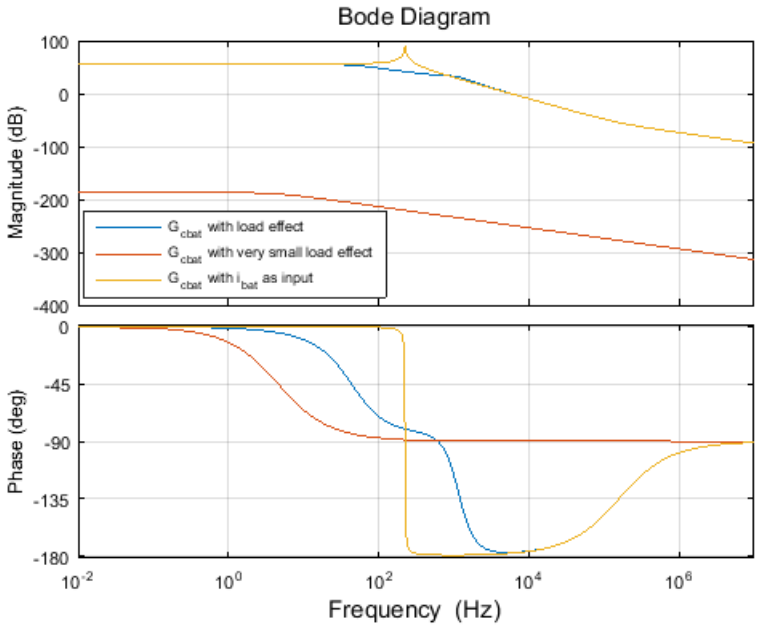

Figure 5.18 *Control-to-battery transfer functions of VF/VO converter*

Characteristics of the converter are still similar to original transfer functions in (5.48) in which battery was realized as current sink. Battery resistance damps the resonant pike which eases the control design. By organizing the CV-controller using the same controller parameters as for both current control schemes, following load affected and original unaffected control loop bode plots are obtained.

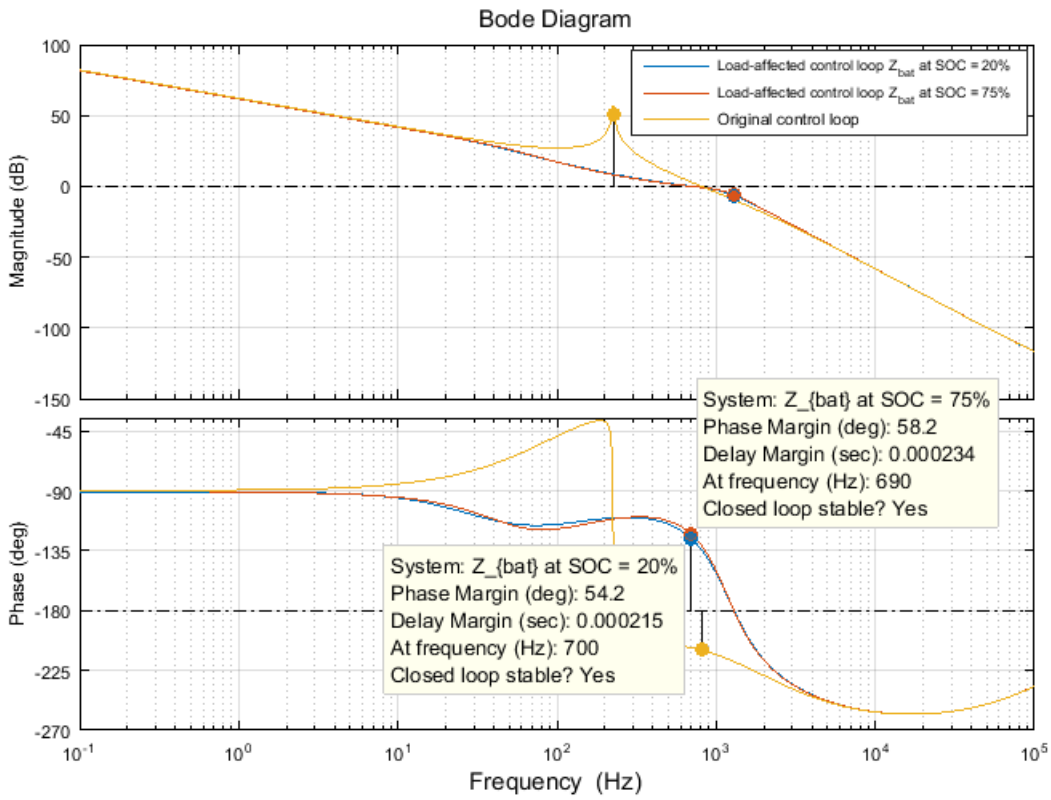

Figure 5.19 *Load-affected control loops at different SOC and original unaffected control loops during buck CV-mode*

It can be seen that the VF/VO converter with derived parameters without load-effect would not be even stable because phase of the control loop is below $-180°$-point. Load-effect with different internal battery impedance now slightly affects to the control loops an increasing impedance reduces the PM by 4°. This is obviously not much but clearly more than with current control schemes. Nevertheless, impedance behaves differently with different battery technologies and increasing impedance may be an issue with larger scale battery storages.

6. SIMULATIONS

The whole simulation model and branch view of the non-linear battery model are shown in figures 6.1 and 6.2

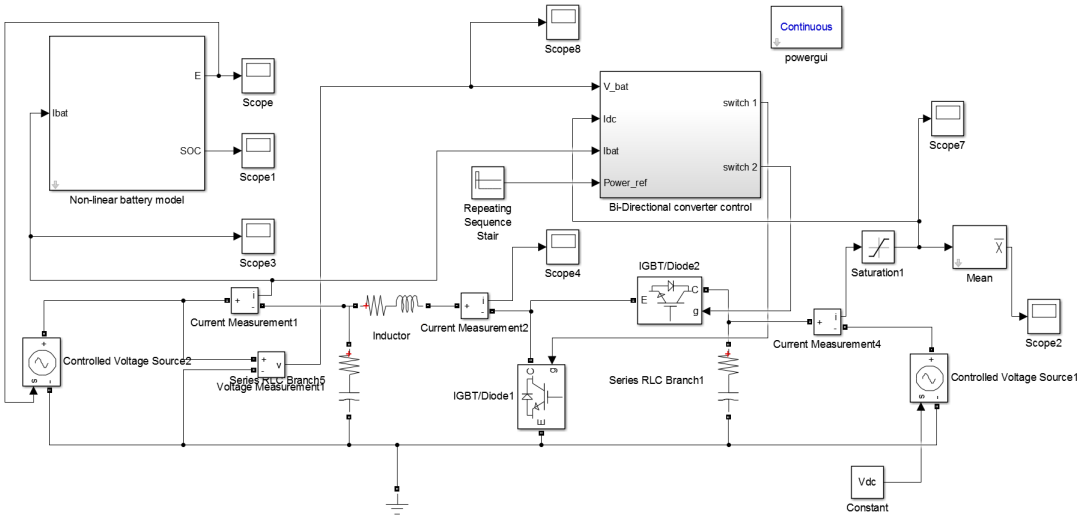

Figure 6.1 *Root view of the used Simulink -model*

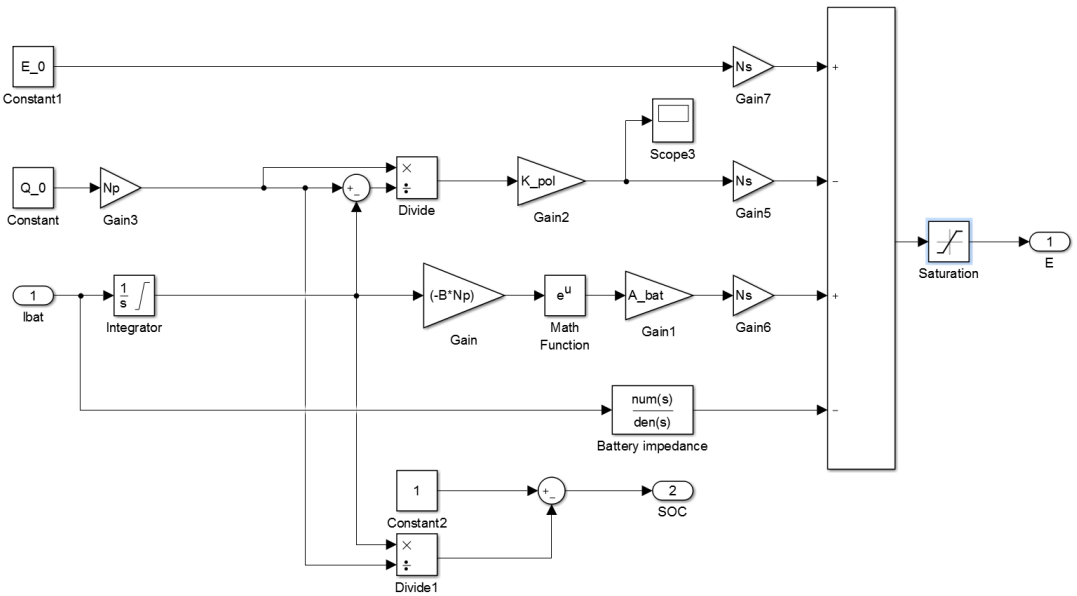

Figure 6.2 *Simulink implementation of the controlled voltage source battery model*

Battery Simulink -model is based on the generic model introduced in section 3.4.3. However, since the available battery pack was for a commercial device, no datasheet was available and also no information about the Lithium-Ion battery chemistry was given. Also the low terminal voltage (36V) was problematic since the real BESS would have a voltage level of several hundred volts. Parameters for the model were eventually obtained from [27] where parameters were stated for a Lithium-Ion cell with nominal voltage of 3.6V. Battery model was derived with 100 cells connected in series with no paraller connection. Capacity was fixed to 2.6Ah. The initial charge of the battery model is adjusted by inserting the wanted charge to integrator's initial condition in the left of the figure 3.4.3. Parameters usable for the model equation (3.8) are shown in table 6.1

$E_0(V)$	$K(V)$	$A(V)$	$B(Ah)^{-1}$	Cells in series (Ns)	Cells in paraller (Np)
$3.7348V$	$0.00876V$	$0.468V$	3.5294	100	1

Table 6.1 *Parameters for the controlled voltage-source battery model*

Control scheme used for the simulations is shown in figure 6.3.

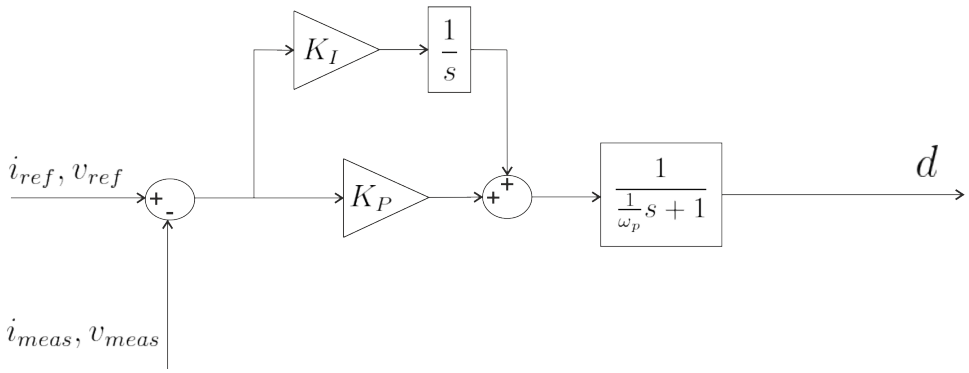

Figure 6.3 *Block diagram of the used control scheme*

Controller is a basic PI-type controller with cascaded first-order low-pass filter that has two poles (one at origo representing an integrator) and one zero. It gives duty ratio as it's output which is further used to create PWM-pulses for the switches. It was also earlier concluded that same control scheme and parameters can be used for all controllers. Controller parameters for all three controllers are shown in table 6.2.

Control mode	ω_z	ω_p	Proportional gain (K_p)	Integral gain (K_I)
Discharge mode	$2\pi 100Hz$	$2\pi 1875Hz$	0.0198	12.45
Charge mode (CC)	$2\pi 100Hz$	$2\pi 1875Hz$	0.0198	12.45
Charge mode (CV)	$2\pi 100Hz$	$2\pi 1875Hz$	0.0198	12.45

Table 6.2 *Parameters for all controllers*

All the used quantities for models derived in this section are presented in table 6.3

V_{bat}	$360V$	C_2	$100\mu F$
V_{DC}	$700V$	r_{C2}	$10m\Omega$
f_{sw}	$15kHz$	V_D	$0V$
L	$5mH$	r_D	0Ω
r_L	$100m\Omega$	r_{DS1}	$70m\Omega$
C_1	$100\mu F$	r_{DS2}	$70m\Omega$
r_{C1}	$10m\Omega$	P_{ref}	$3kW/-3kW$

Table 6.3 *Parameters for converter*

Simulations of a BESS and bi-directional converter are carried out by changing the power reference from $3kW$ to $-3kW$ after 0.2s resulting total time of 0.4s which is simulated. Such a short simulation time was chosen in order to prevent the long simulation time which was noticed due to the algebraic loops in the BESS model. This short time was however regarded appropriate enough to investigate the operation of the control schemes and the effect of changing BESS impedance as the source- and load effect.

6.1 Converter simulations without load- and source effect

Simulated responses obtained for battery current and DC-link current are shown in figure 6.4.

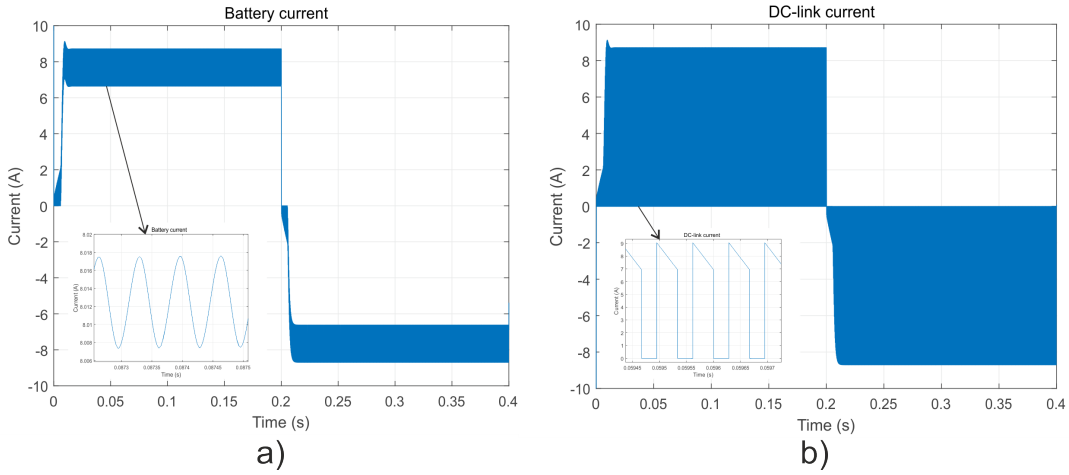

Figure 6.4 *Simulated a) battery current b) DC-link current throughout the simulation*

The zoomed waveforms are shown in the bottom left of the figures above. Current fed to the DC-link is very distorted because DC-link voltage is modeled as constant voltage source. Thus the DC-link capacitor (C2) draws no current according to the relation $i_c = \frac{dv_c}{dt}$ and provides thus no filtering effect. Output current is therefore the same as diode current which is intermittent due to the on- and off-time. It is also very difficult to see the transient behaviour of i_{DC} during power reference changes from it's waveform. This information is also present in the battery current waveform and thus it is used to verify converter operation also during boost mode control. Zoomed view of battery currents after converter is entering boost and buck mode are shown in figure 6.5

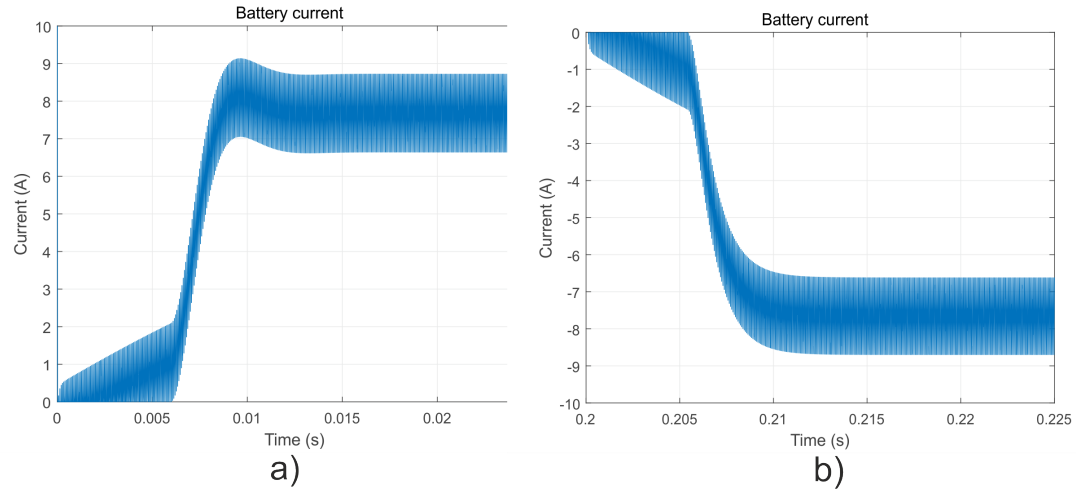

Figure 6.5 *Simulated battery currents zoomed to transient during a) boost-mode CC, b) buck-mode CC*

Simulated responses undergo a DCM operation before entering to CCM which explains the slow response at the beginning of the applied reference change. DCM operation is not further discussed in this thesis. By excluding the slow start-up, it can be concluded that controllers are working properly. It can be seen that boost-mode is experiencing little overshoot while buck-mode is not. This is due to the fact that the use of same controller during different control modes results as slightly different PMs and cross-over frequencies. PM Current during buck operation is negative due to the chosen positive direction of the current which is during boost mode and the response is thus upside down.

6.2 Converter simulations with load- and source effect included

To take the internal impedance into account in the Simulink -model, estimated transfer functions' numerators and denominators are inserted to the transfer function -block named "battery impedance" at the lowest branch in figure 6.2. Battery model must also be initialized to have same SOC as the internal impedance which slightly changes the battery voltage. Also the CV-control is now present and threshold values with battery impedance at 20%-SOC is chosen as $V_{bat-thresh-20\%} = 385V$ and with battery impedance at 75%-SOC is chosen as $V_{bat-thresh-75\%} = 403,7V$. Values were separately chosen to so that the CV-control activated at the same time instant during both simulations which eases the representation of the results. Operation of the converter and battery model is simulated at two different SOC values, at 20% and 75%. Battery current and battery voltage throughout the simulation are shown in figure 6.6.

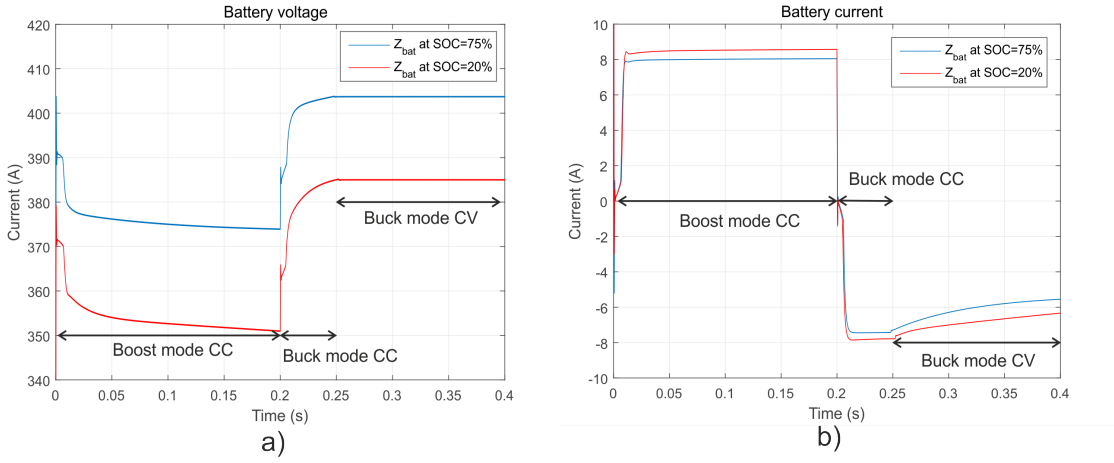

Figure 6.6 *Simulated a) battery voltage, b) battery current throughout the simulation*

Regions in which each control mode is active are also marked in figure 6.6. It can

be concluded that battery current have smaller ripple when load- and source-effect are taken into account in the simulations (compared to a) in figure 6.4). Thus load- and source-effect somewhat damps the converter dynamics.

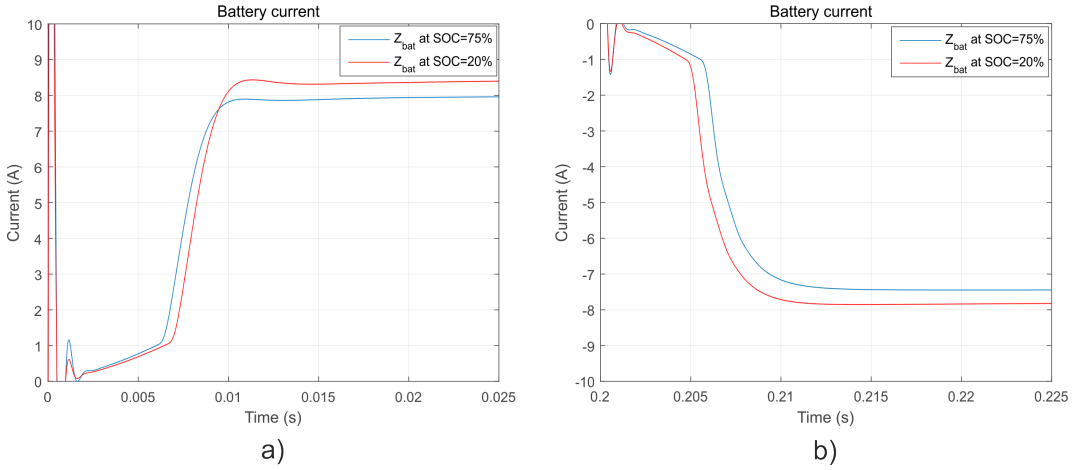

Figure 6.7 *Simulated battery current zoomed at the beginning of a) boost CC-mode b) buck CC-mode with battery internal impedance included*

Set points of the currents are different because the power loss taking place in the increased battery impedance is compensated by increasing the current. Apart from different biases, no changes between the current responses with different battery impedances cannot really be seen from figure 6.7.

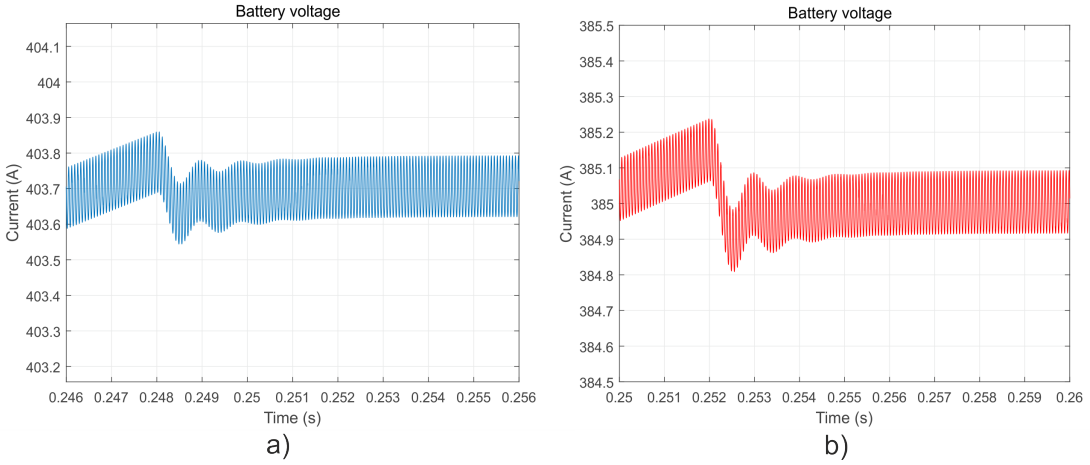

Figure 6.8 *Simulated battery voltage zoomed at the beginning of CV-mode a) battery impedance at SOC=75% b) battery impedance at SOC=20%*

CV-controller activation is delayed due to the artificial delay in the CV-mode sensing algorithm which is why controller is turned on few milliseconds after reaching the

threshold value presented earlier in this section. It can be concluded from figure 6.8 that there is no significant difference between the voltage responses with different impedances. Despite oscillation, controller works fine also on voltage control mode. Thus, it can be concluded that same controller parameters could be used for all control modes.

7. CONCLUSIONS

This thesis is divided into two parts with separate contributions. At first, internal impedance measurement techniques and results from real battery pack have been proposed in this thesis. At second, results were again used to simulate source- and load effect of BESS internal impedance to DC-DC converter between ESS and DC-link of RES. Investigations are made for different control schemes (CC or CV) that should be used when discharging or charging the battery.

Internal impedance of BESS measured with PRBS broadband excitation signal can provide quite accurate information in the frequency range from $10Hz$ to $5kHz$ for both phase- and magnitude responses. This frequency band is useful for SOH estimation since the aging of battery is normally affecting to the internal resistance. Thus, PRBS could be well used to this purpose which is also stated in [6]. Frequencies from $0.1Hz$ to $10Hz$ are however distorted in both magnitude and phase responses and distortion increases as the SOC decreases to 25% and 20%. This is concluded to caused by non-linear behaviour of BESS at these frequencies since adjacent frequency points have same differential trend in all measurements as can be seen from figure 4.8. However, there is same relative trend between PRBS and sine sweep measurements even though the absolute values do not match. Phase response is interfered with the point of irregularity at the point where the two PRBS results are switched. PRBS high-frequency phase response right after the point of irregularity is similar to the sine sweep measurements but low-frequency PRBS is experiencing raising phase with linear slope. This is probably due to the used DAQ-device and it could not been compensated. Despite the observed challenges, PRBS could still be used as relative information at low-frequencies which is useful frequency band for SOC estimation.

Very little research has been made about PRBS and battery measurements [6–8]. Results obtained in this thesis point out that PRBS is potential alternative for battery measurements though there are still problems to be solved. It could easily be integrated into BMS since very little computational effort is required to generate PRBS due to it's binary characteristics. Also measurement time could be significantly reduced since PRBS measures all frequencies in a time determined by

the lowest frequency point while sine sweep measures only the lowest frequency. It is stated in [30] that pure PRBS is suitable for measuring linear systems which is not the case for battery systems. Thus the excitation sequence should be modified to better cope with non-linear systems which can be one way to make improvements to the PRBS measurements results. This will be the focus in the future research.

Due to the deviation in impedance magnitude and phase with PRBS at low frequencies, sine sweep measurements results were used to estimate the impedance parameters in linear transfer function. Derived control loop bode plots during different control modes stated that internal impedance changes the frequency response from unaffected dynamics up to some extend. It however has very little impact on the dynamics of the control loop when internal impedance varies. Similar was also verified by simulations from current and voltage responses during different control schemes. Internal impedance has damping characteristics that reduces the ripple in the battery current compared to simulations without internal impedance. Controllers were here the same for all control modes just to demonstrate that it could be done. Performance could of course be improved by deriving individual optimal controller parameters for each controllers. For CV-control mode, internal impedance is required to make the converter modeling realizable. This is not a problem in reality since it is always included with the battery. Moreover battery internal impedance was observed to have at least no negative impact on the system stability which is normally investigated with source- and load effect analysis [9, 35].

For the simulations, battery was modeled by inserting 100 series-connected cells that has capacity of 2.6Ah. Capacity particularly is too low if any realistic application should be modeled. However, there were problems in modeling the controlled voltage source battery model in Simulink with parallel connected cells to increase the capacity. Therefore only one string of series connected cells were used. Such compromises may have affected to the results but the impact could in that case be even less significant since parallel connection of cells reduces the internal impedance according to the well known circuit theory. Measurement will be carried out to real high capacity battery pack to find out what it really would be for such device. This will be also one big interest in the future research.

BIBLIOGRAPHY

[1] Y. Riffonneau, S. Bacha, F. Barruel, and S. Ploix, "Optimal Power Flow Management for Grid Connected PV Systems With Batteries," *IEEE Transactions on Sustainable Energy*, vol. 2, no. 3, pp. 309–320, 2011.

[2] P. Shaw, P. K. Sahu, S. Maity, and P. Kumar, "Modeling and control of a battery connected standalone photovoltaic system," in *2016 IEEE 1st International Conference on Power Electronics, Intelligent Control and Energy Systems (ICPEICES)*. IEEE, jul 2016, pp. 1–6. [Online]. Available: http://ieeexplore.ieee.org/document/7853123/

[3] R. Singh, S. F. Taghizadeh, and N. M. L. Tan, "Battery energy storage system for PV output leveling based on bidirectional isolated DC-DC converter," in *2013 IEEE Student Conference on Research and Developement*, 2013. [Online]. Available: http://ieeexplore.ieee.org/document/7002548/

[4] X. Zhang, J. Wu, and G. Kang, "SOC estimation of Lithium battery by UKF algorithm based on dynamic parameter model," *2016 13th International Conference on Ubiquitous Robots and Ambient Intelligence, URAI 2016*, pp. 945–950, 2016.

[5] D. I. Stroe, M. Swierczynski, a. I. Stan, V. Knap, R. Teodorescu, and S. J. Andreasen, "Diagnosis of lithium-ion batteries state-of-health based on electrochemical impedance spectroscopy technique," *Energy Conversion Congress and Exposition (ECCE), 2014 IEEE*, pp. 4576–4582, 2014.

[6] A. J. Fairweather, M. P. Foster, and D. A. Stone, "Battery parameter identification with Pseudo Random Binary Sequence excitation (PRBS)," *Journal of Power Sources*, vol. 196, no. 22, pp. 9398–9406, 2011. [Online]. Available: http://dx.doi.org/10.1016/j.jpowsour.2011.06.072

[7] R. Al Nazer, V. Cattin, P. Granjon, M. Montaru, and M. Ranieri, "Broadband identification of battery electrical impedance for HEVs," pp. 2896–2905, 2013.

[8] R. Al Nazer, V. Cattin, P. Granjon, M. Montaru, M. Ranieri, and V. Heiries, "Classical EIS and square pattern signals comparison based on a well-known reference impedance," *World Electric Vehicle Journal*, vol. 6, no. 3, pp. 800–806, 2013.

[9] T. Suntio, *Dynamic Profile of Switched-Mode Converter*. Weinheim, Germany: Wiley-VCH Verlag GmbH & Co. KGaA, mar 2009. [Online]. Available: http://doi.wiley.com/10.1002/9783527626014

[10] T. Suntio, J. Viinamaki, J. Jokipii, T. Messo, M. Sitbon, and A. Kuperman, "Effect of input and output terminal sources on dynamic behavior of switched-mode converters," *2014 International Power Electronics Conference, IPEC-Hiroshima - ECCE Asia 2014*, no. 1, pp. 2240–2246, 2014.

[11] H. Yang, X. Sun, Y. Zhang, Y. Chen, and B. Ren, "Study on coordinate control strategy for photovoltaic generation and hybrid energy storage system," in *Proceedings of the 2016 IEEE 11th Conference on Industrial Electronics and Applications, ICIEA 2016*, 2016, pp. 2339–2344.

[12] M. Trifkovic, M. Sheikhzadeh, K. Nigim, and P. Daoutidis, "Modeling and Control of a Renewable Hybrid Energy System With Hydrogen Storage," *IEEE Transactions on Control Systems Technology*, vol. 22, no. 1, pp. 1–1, 2013. [Online]. Available: http://ieeexplore.ieee.org/lpdocs/epic03/wrapper.htm?arnumber=6477101

[13] A. Etxeberria, I. Vechiu, H. Camblong, and J. M. Vinassa, "Comparison of three topologies and controls of a hybrid energy storage system for microgrids," *Energy Conversion and Management*, vol. 54, no. 1, pp. 113–121, 2012. [Online]. Available: http://dx.doi.org/10.1016/j.enconman.2011.10.012

[14] N. Femia and G. Petrone, "Optimization of perturb and observe maximum power point tracking method," *... , IEEE Transactions on*, vol. 20, no. 4, pp. 963–973, 2005.

[15] A. K. Barnes, J. C. Balda, and C. M. Stewart, "Selection of converter topologies for distributed energy resources," *2012 Twenty-Seventh Annual IEEE Applied Power Electronics Conference and Exposition (APEC)*, pp. 1418–1423, 2012. [Online]. Available: http://ieeexplore.ieee.org/lpdocs/epic03/wrapper.htm?arnumber=6166006

[16] R. Dell and D. Rand, *Understanding Batteries*. Royal society of chemistry, 2001.

[17] V. Pop, H. Bergveld, D. Danilov, P. Regtien, and P. Notten, *Battery Management Systems: Accurate State-of-Charge Indication for Battery-Powered Applications*, ser. Philips Research Book Series. Springer Netherlands, 2008. [Online]. Available: https://books.google.fi/books?id=Qwxrq8tQRSAC

[18] P. Weicker, *A Systems Approach to Lithium-Ion Battery Management*. Norwood, UNITED STATES: Artech House, 2013. [Online]. Available: http://ebookcentral.proquest.com/lib/tut/detail.action?docID=1463546

[19] L. Canals Casals and B. Amante García, "Second-Life Batteries on a Gas Turbine Power Plant to Provide Area Regulation Services," *Batteries*, vol. 3, no. 1, p. 10, 2017. [Online]. Available: http://www.mdpi.com/2313-0105/3/1/10

[20] C. Julien, A. Mauger, A. Vijh, and K. Zaghib, *Lithium Batteries*, 2016. [Online]. Available: http://link.springer.com/10.1007/978-3-319-19108-9

[21] A. R. Sparacino, G. F. Reed, R. J. Kerestes, B. M. Grainger, and Z. T. Smith, "Survey of battery energy storage systems and modeling techniques," in *2012 IEEE Power and Energy Society General Meeting*. IEEE, jul 2012, pp. 1–8. [Online]. Available: http://ieeexplore.ieee.org/document/6345071/

[22] H. B. Vika, "Modelling of Photovoltaic Modules with Battery Energy Storage in Simulink / Matlab Håvard Breisnes Vika," Ph.D. dissertation, Norwegian University of Science and Technology, 2014.

[23] J. E. B. Randles, "Kinetics of rapid electrode reactions," *Discussions of the Faraday Society*, vol. 48, no. 49, pp. 828–832, 1952. [Online]. Available: http://pubs.rsc.org/en/content/articlehtml/1947/df/df9470100011

[24] D. Howey, V. Yufit, and P. Mitcheson, "Impedance measurement for advanced battery management systems," *Procedings of EVS 27 - International Battery, Hybrid and Fuel Cell Electric Vehicle Symposium*, pp. 1–7, 2013. [Online]. Available: http://epg.eng.ox.ac.uk/sites/default/files/Howey/evs27{_}Howey{_}full.pdf

[25] T. Holm, "litiumioniakuston matalat lämpötilat huomioiva impedanssimalli," Ph.D. dissertation, Tampere Univercity of Technology, 2012.

[26] E. Unamuno, L. Gorrotxategi, I. Aizpuru, U. Iraola, I. Fernandez, and I. Gil, "Li-ion battery modeling optimization based on Electrical Impedance Spectroscopy measurements," *International Symposium on Power Electronics, Electrical Drives, Automation and Motion*, pp. 154–160, 2014. [Online]. Available: http://ieeexplore.ieee.org/lpdocs/epic03/wrapper.htm?arnumber=6872015{%}5Cnhttp://ieeexplore.ieee.org/document/6872015/

[27] O. Tremblay, L.-a. Dessaint, and A.-i. Dekkiche, "A Generic Battery Model for the Dynamic Simulation of Hybrid Electric Vehicles," in *2007 IEEE Vehicle*

Power and Propulsion Conference, no. V. IEEE, sep 2007, pp. 284–289. [Online]. Available: http://ieeexplore.ieee.org/document/4544139/

[28] O. Tremblay and L.-a. Dessaint, "Experimental Validation of a Battery Dynamic Model for EV Applications," *World Electric Vehicle Journal Vol.*, vol. 3, pp. 289–298, 2009.

[29] M. Alhanouti, M. Gießler, T. Blank, and F. Gauterin, "New Electro-Thermal Battery Pack Model of an Electric Vehicle," *Energies*, vol. 9, no. 7, p. 563, jul 2016. [Online]. Available: http://www.mdpi.com/1996-1073/9/7/563

[30] K. Godfrey, *Perturbation Signals for System Identification*, 1994.

[31] R. Luhtala, "Adaptive Control of Grid-Connected Inverters Master of Science Thesis," no. March, 2017.

[32] J. A. Abu Qahouq and Z. Xia, "Single-Perturbation-Cycle Online Battery Impedance Spectrum Measurement Method with Closed-Loop Control of Power Converter," *IEEE Transactions on Industrial Electronics*, vol. 0046, no. c, pp. 1–1, 2017. [Online]. Available: http://ieeexplore.ieee.org/document/7884965/

[33] Z. Xia and J. A. Qahouq, "Method for online battery AC impedance spectrum measurement using DC-DC power converter duty-cycle control," *Conference Proceedings - IEEE Applied Power Electronics Conference and Exposition - APEC*, no. 1, pp. 1999–2003, 2017.

[34] B. M. Reddy and P. Samuel, "A comparative analysis of non-isolated bi-directional dc-dc converters," in *2016 IEEE 1st International Conference on Power Electronics, Intelligent Control and Energy Systems (ICPEICES)*. IEEE, jul 2016, pp. 1–6. [Online]. Available: http://ieeexplore.ieee.org/document/7853292/

[35] T. Suntio, J. Viinamaki, J. Jokipii, T. Messo, and A. Kuperman, "Dynamic Characterization of Power Electronics Interfaces," *IEEE Journal of Emerging and Selected Topics in Power Electronics*, vol. 6777, no. c, pp. 1–1, 2014. [Online]. Available: http://ieeexplore.ieee.org/lpdocs/epic03/wrapper.htm?arnumber=6778010

[36] R. D. Middlebrook and Ć. Slobodan, "A general unified approach to modelling switching-converter power stages," *International Journal of Electronics*, vol. 42, no. 6, pp. 521–550, 1977.

[37] L. R. Dung, C. E. Chen, and H. F. Yuan, "A robust, intelligent CC-CV fast charger for aging lithium batteries," *IEEE International Symposium on Industrial Electronics*, vol. 2016-November, pp. 268–273, 2016.